Fluid Drag Reduction with Shark-Skin Riblet Inspired Microstructured Surfaces

Gregory D. Bixler and Bharat Bhushan*

Engineering marvels found throughout living nature continually provide inspiration to researchers solving technical challenges. For example, skin from fast-swimming sharks intrigue researchers since its low-drag riblet microstructure is applicable to many low drag and self-cleaning (antifouling) applications. An overview of shark skin related studies that have been conducted in both open channel (external) and closed channel (internal) flow experiments is presented. Significant work has been conducted with the open channel flow, and less with closed channel flow. The results provide design guidance when developing novel low drag and self-cleaning surfaces for applications in the medical, marine, and industrial fields. Experimental parameters include riblet geometry, continuous and segmented configurations, fluid velocity (laminar and turbulent flow), fluid viscosity (water, oil, and air), closed channel height dimensions, wettability, and scalability. The results are discussed and conceptual models are shown suggesting the effect of viscosity, coatings, and the interaction between vortices and riblet surfaces.

1. Introduction

Inspired by designs found throughout living nature, researchers are reverse engineering the world's flora and fauna to solve technical challenges. Much attention is given to structures and materials since living nature efficiently uses resources and incorporates ingenious designs to survive. Therefore by using lessons from living nature, bioinspired designs are serving as the basis for many new innovations.[1–8]

Two engineering challenges solved in living nature but plaguing a variety of industries are fluid drag[9–13] and fouling.[14–16] Low drag may promote antifouling and vice versa. Drag is the resistant force fluid imposes on an object in either open (external) or closed (internal) channel flow. Drag has many forms, including pressure and skin friction (viscous) drag. In general, pressure drag depends on the streamlined geometry of the object traveling through the fluid, whereas skin friction drag depends on the surface morphology. Biofouling is the accumulation of unwanted biological matter on a surface, with two categories called microfouling (leading to biofilms) and macrofouling. Examples of microfouling organisms include

bacteria and algae, whereas macrofouling include larger barnacles and muscles. In addition to biofouling, inorganic fouling can occur as a result of deposits from corrosion, crystallization, suspended particles, oil, and ice.

Low drag and antifouling applications are plentiful in the medical, marine, and industrial fields. Examples include airplanes, automobiles, wind turbines, ship hulls, microfluidics, medical devices, and pipelines.[11,17–22] Low drag surfaces often equate to less fouling and energy conservation.[20,22–24] For instance, in the oil industry, pipeline flow must overcome high drag due to viscous effects and possibly sludge fouling (with Reynolds numbers reaching 1×10^5). Lower drag in pipelines reduces required pumping energy and increases flow rates. Traditionally, drag is lowered using fluid additives or improving the pipeline interior smoothness with corrosion resistant epoxy coatings.[19,25,26] Such coatings are most effective when sludge fouling is not present, as found with oil flowing from a well at a high temperature and velocity.

In addition to lowering drag, antifouling surfaces can reduce the spread of infectious diseases by limiting biofouling. Medical biofouling occurs in areas such as prosthetic implants, biosensors, catheters, dental implants, and medical equipment. Problems include implant rejection, malfunction of biosensors, and spread of infectious diseases.[27–30] Biofouling is commonly associated with marine environments where noticeable aquatic growth appears on ships and underwater structures. This increases ship hull drag, corrosion, fuel consumption, and engine stress.[15,31–34] Industrial fouling occurs in areas such as power plants, water treatment systems, and food/beverage industries. Problems include pipe blockage, decreased membrane flux, contaminated water, and reduced heat exchanger efficiency.[14,30,35]

In living nature, certain flora and fauna benefit significantly from low drag and antifouling.[5,36–38] In particular, the skin of fast swimming sharks is especially intriguing due to its low drag and antifouling properties. For instance, in the marine environment whales are often covered with barnacles, however sharks remain clean, as illustrated in **Figure 1**. Even though these two marine creatures live in the same environment, the shark seems unaffected by the biofouling. It is believed sharks stay clean due to their microstructured riblets, flexion of dermal denticles, and a mucous layer.[2,39–42] Lower drag is necessary for shark survival, since it allows sharks to swim faster in

G. D. Bixler, B. Bhushan
Nanoprobe Laboratory for Bio & Nanotechnology
and Biomimetics (NLB²)
The Ohio State University
201 W. 19th Avenue, Columbus, OH 43210-1142, USA
E-mail: bhushan.2@osu.edu

**ADVANCED
FUNCTIONAL
MATERIALS**
www.afm-journal.de

Materials Views
www.MaterialsViews.com

Biofouling in the marine environment

Barnacle biofouling on Humpback Whale

Clean shark skin
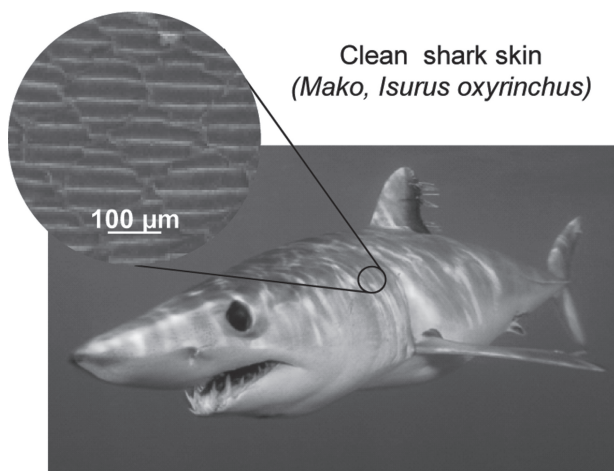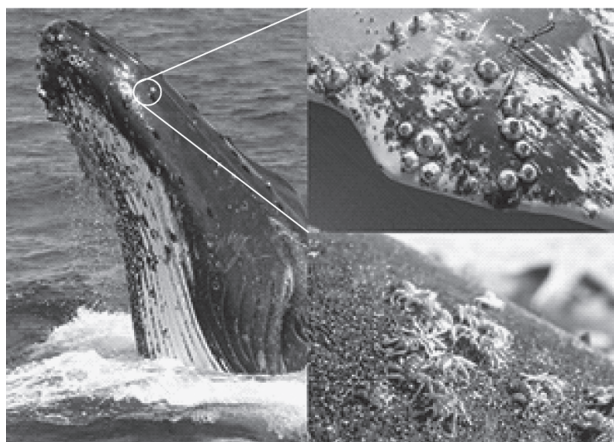*(Mako, Isurus oxyrinchus)*

100 μm

Figure 1. Biofouling in the marine environment. Images highlight differences between Humpback whales and sharks. Even though whales and sharks live in the same environment, barnacle biofouling growth is evident on the whale but not shark skin. It is believed that such antifouling shark skin properties are due to its riblet microtexture, flexion of scales, and a mucous layer. (Top) adapted with permission from www.southbank. qm.qld.gov.au. (Bottom) adapted with permission.[24] Copyright 2012, Royal Society of Chemistry.

Gregory Bixler, P.E. is a mechanical engineering PhD candidate conducting research in the Nanoprobe Laboratory for Bio- & Nanotechnology and Biomimetics (NLB²) at The Ohio State University, Columbus, Ohio. His research interests include biomimetics with a focus on low drag, self-cleaning, and antifouling surfaces found in living nature. Previous industry experience includes Battelle Memorial Institute specializing in machine and product design.

Dr. Bharat Bhushan is an Ohio Eminent Scholar and The Howard D. Winbigler Professor in the College of Engineering, and the Director of the Nanoprobe Laboratory for Bio- & Nanotechnology and Biomimetics (NLB²) at the Ohio State University, Columbus, Ohio. He holds two M.S., a Ph.D. in mechanical engineering/mechanics, an MBA, and two honorary and two semihonorary doctorates. His research interests include fundamental studies with a focus on scanning probe techniques in the interdisciplinary areas of bio/nanotribology, bio/nanomechanics and bio/nanomaterials characterization and applications to bio/nanotechnology, and biomimetics. He is currently a visiting professor at KFUPM, Saudi Arabia, Harbin Inst. Tech, China, Univ. of Kragujevac, Serbia and University of Southampton, UK.

order to catch prey.[40,41,43] The subsequent increased fluid flow velocity at the skin reduces microorganism settlement time and promotes antifouling.[37,38,42] In addition, microorganisms larger than the spacing between riblets are unable to effectively adhere to and ultimately colonize the skin, which further promotes antifouling.[5,44–46]

Low drag and antifouling surfaces have been the subject of much experimentation using shark skin riblet-inspired microtextured surfaces. An ideal surface would withstand harsh environments, adhere to a variety of substrates, combine both low drag and antifouling properties, and be relatively inexpensive.

Determining the optimal riblet surface morphology for maximum drag reduction has been the focus of many efforts. Experimental results indicate that shark skin inspired surfaces

effectively reduce drag in open and closed channel flow, although limited data is available with closed channel. Furthermore, closed channel experiments have been conducted to study the neighboring wall effects by using so-called microsized closed channels. In open channel, drag has been measured using water,[47–51] oil,[52–55] and air.[39,53,56–64] Similarly, in closed channel flow, drag has been measured using water,[47,51,65,67] oil,[68] and air.[67,69,70] Both drag (for open channel) and the pressure drop (for closed channel) measurements characterize the riblet drag reduction efficiency.

Previous experiments have utilized a variety of riblet geometries, configurations, materials, fluids, and flow conditions (laminar and turbulent flow). Geometries include blade, sawtooth, scalloped, and bullnose geometries with continuous and segmented (aligned and staggered) configurations in water, oil, and air. Open channel oil experiments with metal riblets show drag reduction of nearly 10%,[52] whist closed channel

Materials
Views

www.MaterialsViews.com

ADVANCED
FUNCTIONAL
MATERIALS
www.afm-journal.de

FEATURE ARTICLE

water experiments with polymer riblets show pressure drop reduction up to 34%.[67] Shark skin replicas have also been evaluated, and have reduced pressure drop up to 30% in closed channel water flow.[24,66]

Larger scale drag reducing efforts have included the experimental 3M Corp. (Minneapolis, MN) vinyl riblets as well as the commercially available Speedo brand FastSkin fabric racing swimsuit. Such riblet technology has captured the attention of the National Aeronautics and Space Administration (NASA), U.S. Department of Energy, U.S. Navy, Airbus, Boeing, as well as Olympic competitors. In the 1984 Los Angeles Olympics and 1987 America's Cup, 3M riblets were applied to U.S. boats, which presumably helped to secure victories. The 2008 Beijing Olympics witnessed the benefit of the Speedo FastSkin swimsuit when American Michael Phelps set Olympic records and won several gold medals. Reportedly, the swimsuits reduce drag up to 4% for men and 3% for women.[71]

Here, we present an overview of shark skin related studies that have been conducted in both open channel (external) and closed channel (internal) flow experiments. Significant work has been conducted with the open channel flow, and less with closed channel flow. Results provide design guidance when developing novel low drag and self-cleaning surfaces for applications in the medical, marine, and industrial fields. Experimental parameters include riblet geometry, continuous and segmented configurations, fluid velocity (laminar and turbulent flow), fluid viscosity (water, oil, and air), closed channel height dimensions, wettability, and scalability. Results are discussed and conceptual models are shown suggesting the effect of viscosity, coatings, and the interaction between vortices and riblet surfaces.

2. Fluid Drag Reduction

In this section, we present fluid drag mechanisms, which include pressure and skin friction drag. Next, we present the mechanisms at work with the low drag skin of sharks.

2.1. Drag Mechanisms

Drag is commonly categorized into pressure and skin friction drag, where the shark skin riblet microstructures generally reduce the skin friction drag. Describing pressure drag is best accomplished by imagining walking through a pool of water, where the resistance is primarily due to the pressure or form drag. The pressure drag is the drag that occurs due to the required energy necessary to move the fluid from the front to the back of the object, such as water moving around the one's legs. This drag may be reduced with streamlined shapes, such as airfoil designs common to aircrafts. Conversely, skin friction or viscous drag is the drag that occurs due to the interaction of the closest fluid layer to the object's surface, such as the skin of the one's legs in the water. This drag is due to the attraction of fluid molecules to the surface, which creates friction and thus resistance. Away from the surface the velocity of the molecules increases until the fluid achieves the mean fluid flow velocity. Higher viscosity fluids exhibit higher drag due to the higher attraction between fluid layers, which then leads to increased skin friction.[9–13]

Laminar and turbulent boundary layers help describe fluid flow, where turbulent boundary layers lead to higher skin friction drag. The boundary layer is the fluid layer adjacent to the surface, with the innermost layer called the viscous sublayer. In this layer, laminar flow appears smooth and orderly whilst turbulent flow appears random and chaotic. Additionally, laminar flow is controlled by viscous forces between the fluid molecules whereas turbulent flow is controlled by inertial forces. Turbulent vortices in the viscous sublayer naturally translate in the cross flow and streamwise directions, which leads to vortices intermingling and ejecting from the viscous sublayer. This movement increases momentum transfer and shear stress, which results in higher drag.[72,73] Therefore, laminar flow is preferred for low drag; however in many real-world fluid flow applications, the boundary layers naturally transition from laminar to turbulent. This transition can be described with the dimensionless Reynolds number (Re), which is the ratio of inertial forces to viscous forces, or:[12]

$$Re = \frac{V D}{v} \tag{1}$$

where V is the fluid mean flow velocity, v the fluid kinematic viscosity, and D is the characteristic length which is the hydraulic diameter (for closed channel) or a distance downstream from the leading edge (for open channel).[12] For a rectangular closed channel, $D = 4A/c$, where A is the cross sectional area and c is the wetted perimeter. Transition from laminar to turbulent flow depends on parameters in Equation 1 as well as surface roughness and freestream disturbances, where such features may "trip" the boundary layer to become turbulent. Such transition occurs around $Re = 2300$ for closed channel and $Re = 500\,000$ for open channel flow.[12,13]
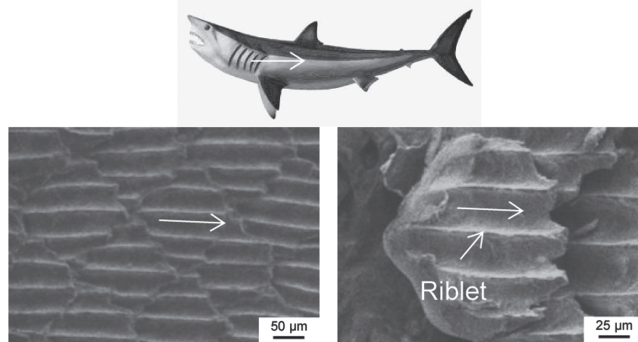
2.2. Shark Skin

Shark skin is designed with microstructured features that effectively control naturally occurring turbulent vortices, which leads to less momentum transfer and shear stress, and thus reduces drag. Therefore much attention has been given to actual shark skin and the mechanisms at work. The skin of fast swimming sharks (such as Mako, *Isurus oxyrinchus*) is covered with scales called dermal denticles, which contain specially sized and spaced riblets oriented parallel to the swimming direction. Dermal denticles from both the Mako and Spiny Dogfish shark species are shown in **Figure 2**, with the flow direction indicated by the arrows. The shape and size of the dermal denticles as well as the number of riblets varies between shark species. Riblets can also vary between different locations on the same shark.[5,41,43,53] However riblets operate on similar principles, where low drag is achieved by efficiently directing water at the solid-liquid interface.

The microstructured riblets encourage anisotropic flow as well as control vortices on the skin naturally present in turbulent flow. The riblets lift and presumably pin any vortices generated in the viscous sublayer, which leads to lower drag. Images in **Figure 3** show flow visualization experimental results using smoke from atomized oil burned in air, both with and without riblets, and at two different velocities (V). Shown are the dimensionless riblet lateral spacing (s^+) and height (h^+) parameters, which provide helpful guidance to riblet optimization,
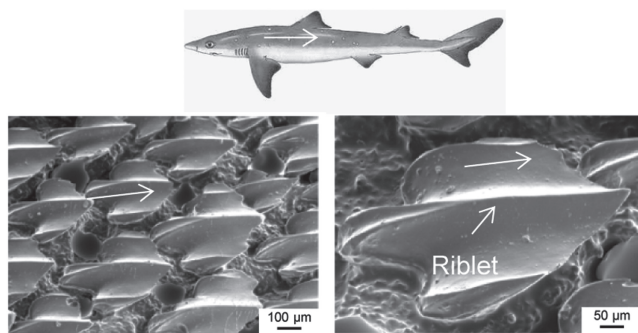
SEM micrographs of shark skin samples from living nature

Actual shark skin (Mako, Isurus oxyrinchus)

Riblet

50 μm

25 μm

Dermal denticle

Replica shark skin (Spiny Dogfish, Squalus acanthias)

Riblet

100 μm

50 μm

Dermal denticle

Flow visualization of vortices interacting with flat and riblet surfaces using smoke in air from atomized oil (flow into the page)

Drag decreasing V = 3 m/s   Drag increasing V = 5 m/s

Vortice

Flat plate

Drag decreasing V = 3 m/s   Drag increasing V = 5 m/s

h+ = 12.6

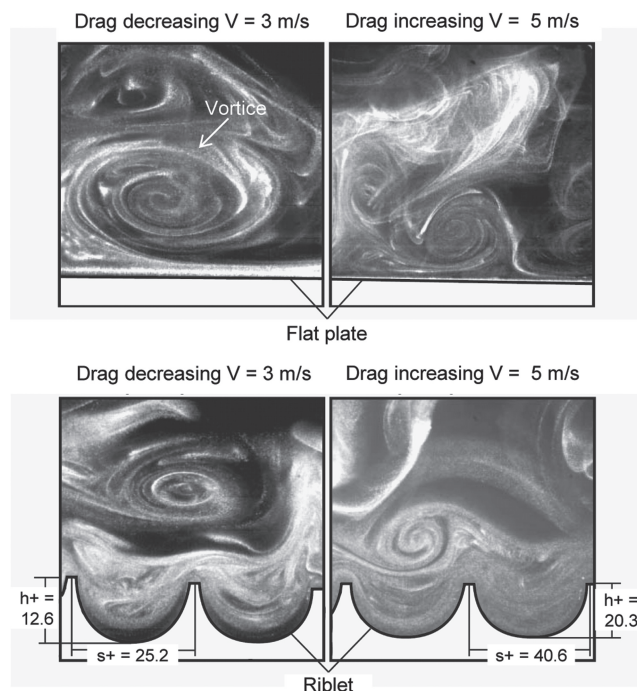h+ = 20.3

s+ = 25.2

s+ = 40.6

Riblet

Figure 3. Flow visualization images using smoke from atomized oil burned in air to study the turbulent vortices behavior with and without riblets at two velocities. Top images show the vortices on a flat plate with a relatively large amount of surface contact area, which leads to higher drag. Bottom images show the vortices are lifted above the riblet tips, with a relatively small amount of surface contact area, which leads to lower drag. The dimensionless parameters for height ($h+$) and spacing ($s+$) aid in the understanding of riblet design for any flow condition. Such parameters are based on riblet spacing or height, fluid kinematic viscosity, and wall shear stress velocity. Adapted with permission.[76] Copyright 2001, Springer.

Figure 2. SEM images of shark skin samples from living nature. Actual Mako (top) (adapted with permission.[24] Copyright 2012, Royal Society of Chemistry.) and replica Spiny Dogfish (bottom) (adapted with permission.[66] Copyright 2010, Institute of Physics.) Shark skin images are shown at two magnifications. These highlight the scales (dermal denticles) and riblets which are responsible for low drag and antifouling properties. Arrows indicate fluid flow direction.

as described in the following section. The images suggest that with appropriately sized riblets, vortices are lifted above the surface and presumably pinned at the riblet tips. Lifting reduces the total shear stress since vortices contact just the small riblet tips (as opposed to the total surface area). Pinning is believed to reduce the cross-stream motion of fluid (i.e., provides anisotropic flow) and ejection of vortices from the viscous sublayer, which reduces momentum transfer.[39–42,52,53,74–77] Turbulent vortices are also present in fluids besides water; therefore the shark skin inspired riblets are expected to provide a similar drag-reducing benefit with any fluid such as air and oil.

2.3. Riblet Optimization

In addition to experimenting with actual shark skin or replicas, research has been conducted by fabricating shark skin inspired

artificial riblets. Such riblets represent those found on actual shark skin; however their shape and size differ in order to optimize the tradeoff between drag reduction and feasible manufacturing techniques. Optimizing riblet geometries is twofold; one is to lift and pin vortices, and the other is to minimize drag (skin friction) due to the riblets themselves. Since riblets protrude into the flow channel, the increased surface area equates to increased drag. In order to optimize drag reduction, the riblets should lift and pin the vortices as well as encourage anisotropic flow along the surface. Such efficient flow is found by considering each valley between riblets and minimizing the wetted perimeter, since increased wetted perimeter leads to increased drag.

Another consideration for riblet optimization includes utilizing dimensionless parameters (measured in wall units). These are denoted by the + symbol, which allow for better comparison of experiments with various riblet geometries and flow conditions. Minimizing energy losses can be accomplished with riblets that effectively lift and presumably pin the turbulent vortices. In general, skin friction or viscous drag increases with

www.MaterialsViews.com

ADVANCED
FUNCTIONAL
MATERIALS
www.afm-journal.de

FEATURE ARTICLE

higher Reynolds numbers, which is related to energy dissipated through heat loss. As shown in Equation 1, length multiplied by mean flow velocity and divided by kinematic viscosity provides the Reynolds number. Similarly, Reynolds numbers based on riblet parameters can also be calculated, which are useful for riblet optimization. Important riblet parameters include spacing (s), height (h), and thickness (t), which are described below.

The Reynolds numbers based on spacing and height of the riblets are defined as:[52–53,72,78]

$$s^+ = \frac{s\,V_\tau}{v} \qquad (2)$$

$$h^+ = \frac{h\,V_\tau}{v} \qquad (3)$$

The Reynolds numbers based on thickness is being defined here as:

$$t^+ = \frac{t\,V_\tau}{v} \qquad (4)$$

where V_τ is the wall shear stress velocity.

Considering kinetic energy, the wall shear stress expression $\tau_o = \rho V_\tau^2$ provides the wall shear stress velocity as:[52–53,72,78]

$$V_\tau = \left(\frac{\tau_o}{\rho}\right)^{1/2} \qquad (5)$$

where ρ is the fluid mass density.

For pipe flow, the approximate wall shear stress (τ_o) can be found by combining the Blasius and Fanning friction factor formulas.[52–53,72,78] The Blasius formula describes the coefficient of friction for turbulent flow as:[12]

$$c_f = 0.0791(Re)^{-1/4} \qquad (6)$$

The Fanning friction factor formula describes the coefficient of friction for laminar flow as:[12]

$$c_f = \frac{2\tau_o}{\rho V^2} \qquad (7)$$

Combining the two above equations and solving for wall shear stress yields:

$$\tau_o = 0.03955\, v^{1/4}\, \rho\, V^{7/4}\, D^{-1/4} \qquad (8)$$

Determining optimal riblet dimensions for various flow conditions is possible by considering dimensionless parameters. For instance, the optimized riblet spacing for a given fluid can be determined by rewriting Equation 2 where $s = s^+ v / V_\tau$. This equation indicates that for a constant s^+ value, the required riblet spacing for maximum drag reduction increases as kinematic viscosity (v) increases.[52,53,79] Appropriate s^+ values may be determined by varying the riblet spacing with a constant flow velocity or vice versa, where varying velocity is generally more feasible. Experimental results will be presented later indicating that an s^+ near 15 is optimal for maximum drag reduction with various riblet geometries.[52,80] Furthermore, it will be shown later that a correlation exists between riblet spacing, vortex diameter, and vortex lateral spacing.

Visualizing the interaction between riblets and vortices provides insight in order to optimize riblets. Turbulent flow visualization experiments indicate that vortices equal approximately 35–50 wall units in diameter (shown in Figure 3). Additionally, these measurements are verified with experiments using dye in water[72] and analysis of the turbulent boundary layer.[81] Such dimensions are important in order to optimize riblet spacing. For experiments shown in Figure 3, velocities $V = 3$ m/s and 5 m/s produce s^+ values equaling 25.2 and 40.6, respectively. As presented, the $V = 3$ m/s case shows drag decreasing, whereas the $V = 5$ m/s case shows drag increasing. In the $V = 3$ m/s case, vortex diameter is larger than s^+, which leads to lifting the vortex, thus lowering drag. However for the $V = 5$ m/s case, the vortex diameter is about the same as s^+, therefore providing less vortex lifting, thus leading to higher drag. Furthermore, velocities $V = 3$ m/s and 5 m/s produce h^+ values equaling 12.6 and 20.3, respectively. For constant h/s, h^+ increases with s^+, which then further increases the contact area between vortices and riblets; thus leading to higher drag.

Therefore an s^+ near 15 with $h/s = 0.5$ corresponds to approximately three riblets per vortex, where vortices are believed to remain lifted and presumably pinned about the riblet tips. Both s^+ and h^+ information is useful in order to determine relationships between drag, fluid viscosity, and riblet dimensions. Such information allows for scaling riblets for turbulent drag reduction and comparing experimental results.

3. Riblets and Experimental Methods

In this section, we first provide an overview of the various riblet designs and configurations. Next we present various fabrication techniques utilized to create riblets as well as their advantages and disadvantages. Finally we describe the experimental procedures for open and closed channel experimentation using water, oil, and air.

3.1. Riblet Geometries and Configurations

Shark skin dermal denticles and riblets exhibit rather complex three dimensional geometries and configurations, therefore fabrication of such microstructured features is challenging. Additionally, in order to study the dimensional effects of riblets in fluid flow, experiments with varying sizes of relatively durable fluid-tolerant riblets are necessary. However due to the microsized nature of the riblets, this poses difficulty in producing cost effective riblet samples, especially for larger sample sets. In response, the assumingly most important characteristics of the riblets have been identified, and then samples have been fabricated for experimentation.

Riblet sizes range from species to species and from location to location on sharks. For reference, the Spiny Dogfish shark *Squalus acanthias* has triangular shaped riblets with a base width of 100 to 300 μm, summit radius of about 15 μm, height of 200 to 500 μm, and spacing of 100 to 300 μm.[66] Using actual riblets for inspiration, simplified artificial riblet samples include various combinations of blade, sawtooth, scalloped, and bullnose geometries with continuous and segmented (aligned and staggered) configurations. It is believed that actual shark skin most closely resembles scalloped riblets with a staggered

**ADVANCED
FUNCTIONAL
MATERIALS**

www.afm-journal.de

Materials Views

www.MaterialsViews.com

Shark skin inspired riblet geometries and configurations

Geometries
(cross sectional views)

Configurations
(top views)

Blade

Continuous

Sawtooth

Aligned segmented

Scalloped
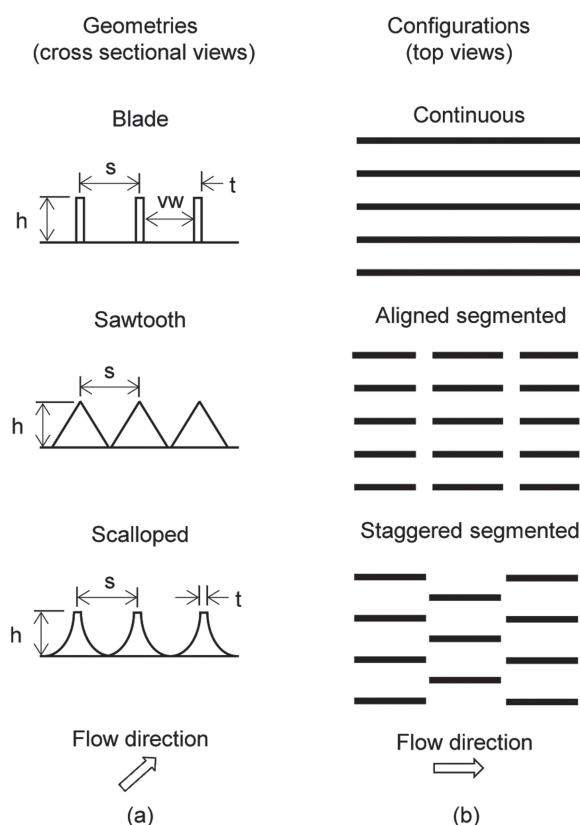
Staggered segmented

Flow direction

(a)

Flow direction

(b)

Figure 4. Typical shark skin inspired riblet geometries and configurations that have been experimentally evaluated. Shown are a) blade, sawtooth, and scalloped geometries as well as b) continuous, aligned segmented, and staggered segmented configurations. Actual shark skin most closely resembles the scalloped geometry and staggered segmented configuration.

segmented configuration. Schematics of simplified riblets fabricated for experimentation are illustrated in **Figure 4**, with typical geometries and configurations. Dimensions of interest include riblet height (h), spacing (s), thickness (t), and valley width (vw); and their importance will be discussed in the results section. Open and closed channel experiments and their subsequent geometries and configurations are summarized in **Tables 1–3**.

3.2. Riblet Fabrication

Riblets have been fabricated with a variety of polymers and metals using various fabrication and assembly processes. The actual process depends on many factors, such as costs, geometry/configuration, durability, precision, accuracy, base material, experimental set-up, chemical compatibility, and sample set size. Feasible riblet fabrication techniques include using metal shims,[52] machined acrylic,[52,89] machined aluminum,[57] extruded/coextruded polymer,[17] embossed polymer,[17] soft lithography,[24,66] photolithography,[46] wet and dry etching,[46] grinding,[90] rolling,[91] and laser etching.[67,68,92] In general, blade and scalloped riblets are less durable than sawtooth riblets, and

Table 1. Open channel riblet experimentation.

Fluid	Riblet design	Riblet configuration	Riblet material	Maximum turbulent drag reduction	Ref.
Water	Sawtooth	Continuous	Polymer	8%	[47]
	Sawtooth	Continuous	Vinyl	9%	[51]
	Sawtooth	Continuous	Vinyl	6%	[49]
	Sawtooth	Continuous	Vinyl	13%	[50]
	Sawtooth	Continuous	Polymer	7%	[48]
Oil	Blade, sawtooth & scalloped	Continuous	Brass & Plexiglas	9.9%	[52]
	Blade	Staggered segmented	Brass	7%	[53]
	Blade	Continuous	Titanium & nickel	4.9%	[54]
	Sawtooth	Continuous	Polyurethane	7.6%	[55]
Air	Blade	Continuous	Metal & polymer	8.5%	[58]
	Blade	Staggered segmented	Epoxy	7%	[53]
	Sawtooth, scalloped & bullnose	Continuous	Aluminum & vinyl	8%	[56]
	Sawtooth, scalloped & bullnose	Continuous	Aluminum & vinyl	8%	[57]

continuous riblets are easier to fabricate than segmented. Furthermore, photolithography is preferred for producing the most accurate two-dimensional riblet geometries, but can be cost prohibitive.

The 3M Corp (Minneapolis, MN) produces an experimental vinyl adhesive backed riblet sheet, which has been used in many

Table 2. Closed channel riblet experimentation.

Fluid	Riblet design	Riblet configuration	Riblet material	Maximum turbulent pressure drop/drag reduction	Ref.
Water	Blade	Aligned segmented	Acrylic	23%[a]	[66]
	Blade & sawtooth	Aligned segmented & continuous	Vinyl & acrylic	22%[a]	[67]
	Sawtooth	Continuous	Vinyl	9%	[51]
	Sawtooth	Continuous	Polymer	28%	[47]
	Sawtooth	Continuous	Vinyl	7%	[65]
Oil	Blade	Aligned segmented & continuous	Acrylic	7%[a]	[68]
Air	Blade	Continuous	Polymer	3%	[69]
	Blade & sawtooth	Aligned segmented & continuous	Vinyl & acrylic	11%[a]	[67]
	Sawtooth	Continuous	Epoxy	7%	[70]

[a] Microsized channel

www.MaterialsViews.com

ADVANCED
FUNCTIONAL
MATERIALS
www.afm-journal.de

FEATURE ARTICLE

Table 3. Sawtooth riblet airfoil experimentation.

Reynolds number	Airfoil cross sec-tion description	Airfoil type	Sawtooth riblet size with $h = s$ [μm]	Riblets applied to longitudinal location/chord length	Trip applied to longitudinal location/chord length	Angle of attack	Maximum drag reduction	Ref.
17 000	Symmetric		180	0–100%	n/a	0°	4.3%	[63]
250 000	Symmetric		23, 76, 152	10–100%	n/a	0°	13.3%	[82]
530 000–790 000	Thin		76, 152	20–95%	2.5%	0°	2.7%	[59]
750 000	Thin		114	12–96%	10%	0–6°	6%	[83]
1 000 000	Symmetric		76, 152	12–96%	10%	0–6°	13%	[84]
1 000 000	Thin		76	12–96%	10%	0–12°	10%	[60]
1 000 000	Thin		76	12–96%	10%	0–12°	14%	[60]
1 000 000	Thick		114	5–100%	5%	0°	5%	[85]
1 000 000–1 850 000	Thick		44, 62, 100, 152	40–100%	n/a	0°	5%	[64]
3 000 000	Thick		18	15–100%	6%	-0.5–1°	10%	[86]
3 300 000	Thin		17, 23, 33, 51	15–100%	n/a	0°	3.3%	[87]
2 000 000–6 000 000	Symmetric		44, 100, 152	0–100%	5%	0°	7%	Present work
4 900 000–22 300 000	n/a		33, 51, 76	87% coverage	n/a	0°	4%	[88]

fluid drag studies. The riblet cross sectional shape consists of equilateral triangles (sawtooth geometry) where the height (*h*) equals the spacing (*s*), as illustrated in Figure 4 and **Figure 5**. Sizes range from 44 to 150 μm. These sawtooth riblets have

Riblet drag reduction experiments

SEM of sawtooth riblet film

Airfoil with riblet film covering upper and lower surfaces

Section A-A (not to scale)

Air flow

Trip strips (x2)

Leading edge

Angle of attack

Chord

Camber of Upper Surface

Camber of Lower Surface

Trailing edge

Figure 5. Riblet drag reduction experiments on airplanes and airfoils. In flight tests, total fuel consumption determines the amount of drag reduction. SEM image shows the sawtooth riblet cross section, where riblet grooves are oriented parallel to the fuselage. Section A-A illustrates a typical airfoil. Adapted with permission.[64] Copyright 2011, American Institute of Aeronautics and Astronautics.

many advantages such as ease of installation onto large flat or curved surfaces and high durability. The sheets are reported to be either coextruded through a die capable of a patterned surface or more likely embossed with a negative master mold using heat and/or pressure.[17]

In addition to riblet geometries and configurations, researchers have examined the effect of applying coatings to alter wettability properties. For instance, studies suggest that super-hydrophobic surfaces exhibit lower water drag[5,20,24,66,67,93–96] and self-cleaning[5,20,24,97] properties, which are believed to promote antifouling. Furthermore, another study suggests that superoleophilic and possibly superoleophobic surfaces can also reduce oil drag.[68] In a recent study, a nanostructured coating was created with silica particles and applied to laser etched polymer riblets[67] using a specified dip-coating method with nano particles suspended in a resin binder.[98,99] This coating is believed to actually improve the smoothness of milled or laser etched riblets, which may be desirable for air flow.
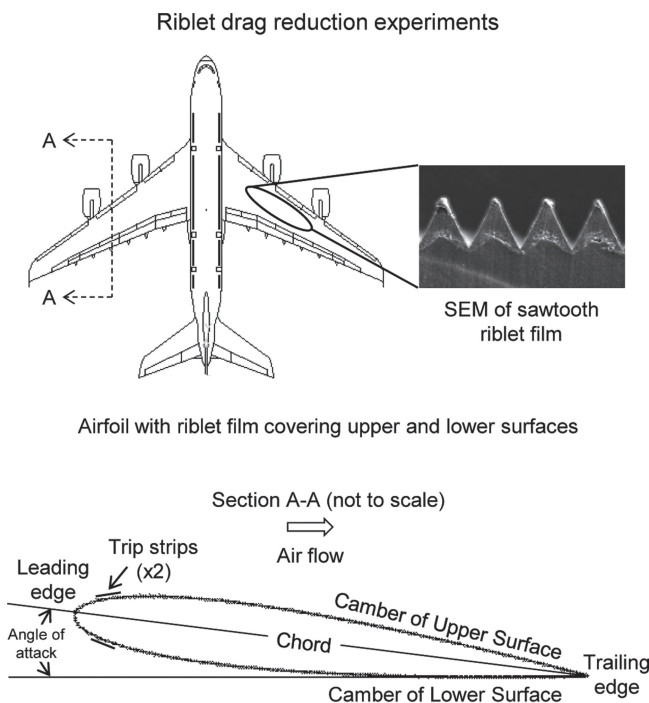
3.3. Drag Measurement Techniques

In this section, we present the various methods to evaluate riblets in water, oil, and air in both open and closed channel experiments. Within each of these experimental set ups includes descriptions of the various drag measurement techniques.

3.3.1. Open Channel

Measuring drag in open channel is conducted with water and oil channels as well as in wind tunnels. Various methods include using force balances and wake traverses, depending on the fluid and application. For instance, force balances measure water, oil, and air drag; whereas wake traverses measure wind tunnel airfoil drag.[61,100] Riblets have also been evaluated on

airplanes during flight tests, with riblets covering a portion of the wing and fuselage sections, as shown in Figure 5. Total fuel consumption is measured during the riblet flight tests in order to evaluate the total amount of drag reduction.[61]

A typical force balance method for open channel experimentation is illustrated in **Figure 6**a, where flat sample plates mounted on a force balance are lowered into the moving liquid (typically water or oil). The flow rate is maintained with a flow channel set-up as illustrated in Figure 6b, with much research conducted using the so-called Berlin oil channel.[79] Propeller driven flow provides a constant current in order to measure the drag resistance force on the sample plates. The percentage drag reduction is calculated using the dimensionless expression $\Delta\tau/\tau_o$ (%), where $\Delta\tau$ is the difference between measured shear stresses on the riblet sample (τ) and the smooth (τ_o) surfaces.

Typical wake traverse and force balance methods for wind tunnel experimentation are also illustrated in Figure 6a. Many experiments have been conducted with subsonic tunnels, whereas fewer with the transonic or supersonic tunnels. A transonic wind tunnel design is illustrated in Figure 6b, which highlights the transverse wake probe and infrared camera locations. High pressure air in holding tanks is suddenly released into the settling chamber, which then flows across the airfoil sample at a known constant speed. Drag is measured using a traversing wake probe, which measures pressure by traversing downwind from the airfoil during experimentation. The probe measures the pressure in the airfoil wake, and when compared with a smooth airfoil is used to calculate the percentage drag reduction. The drag coefficient (C_d) is calculated with the wake integral expression using velocity calculated from the wake pressure profile.[101–103] The percentage drag reduction is calculated using the dimensionless expression ΔC_d (%), which is the difference between drag coefficient on the riblet sample and the smooth surfaces. For completeness, C_d is expressed as:[12]

$$C_d = \frac{F_d}{0.5\rho V^2 A_W} \tag{9}$$

where F_d is the drag force and A_w is the total surface area in contact with the fluid (or wetted area).

A symmetric airfoil cross section is shown in Figure 5 with riblets applied to the upper and lower camber from the leading to trailing edges. Flow in a boundary layer over an airfoil may begin laminar, and then transition to turbulent depending on surface roughness or freestream disturbances. Trip strips help ensure the transition of laminar to turbulent flow at a particular location, which allows for a more direct comparison of experiments when the turbulent coverage is known.[102,103] Airfoil geometries vary in design, as shown in **Figure 7** with thin, thick, curved thin, reflex trailing edge, and symmetrical wing section options. Such geometries allow for low drag, high speed, low lift, and high drag when necessary. A summary of wind tunnel experiments is shown in Table 3, which presents airfoil designs with designations such as NACA 0012 and GAW-2 for applications such as aircraft wings and wind turbines, respectively.

In wind tunnel experiments, riblet covered airfoils have been evaluated on over a wide range of speeds and angle of attacks. Accounting for compressibility effects, speed is defined as the Mach number (Ma), with subsonic (Ma < 0.75), transonic (0.75 < Ma < 1.2), and supersonic (1.2 < Ma < 5) designations.

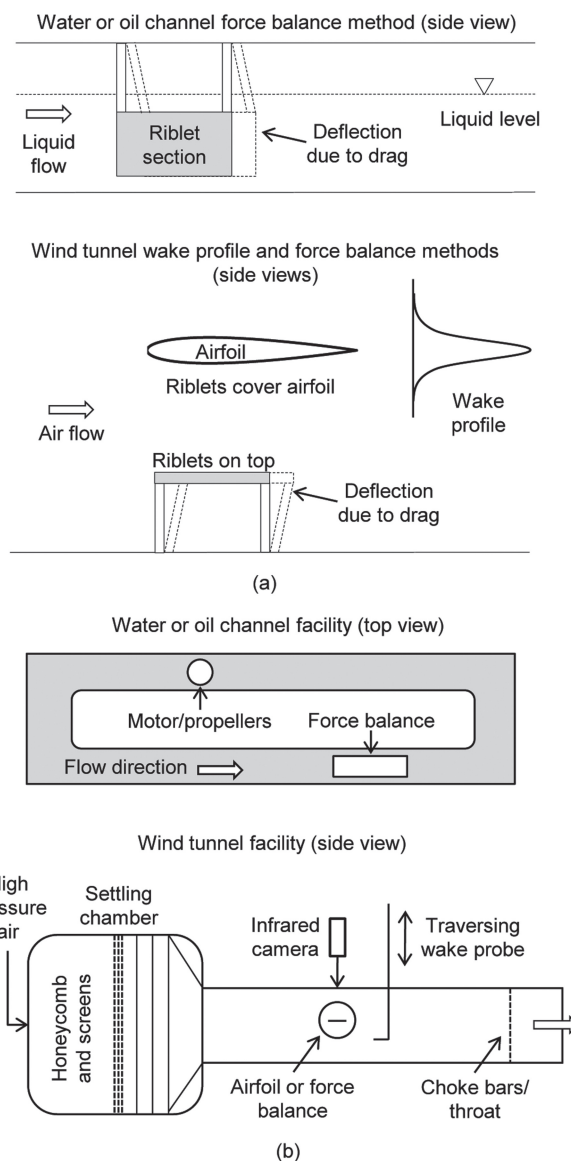Methods (a) and facilities (b) to measure open channel drag with water, oil, and air

Figure 6. Open channel methods and facilities to measure drag using water, oil, and air. a) In water or oil channel flow, riblets are applied to a force balance plate that is lowered into the moving fluid (top). The deflection of the force balance translates into the total amount of drag. In airfoil experiments (bottom), the wake profile determines the total amount of drag. Drag may also be measured with riblets applied to a flat plate or airfoil using a force balance in the wind tunnel. b) Open flow channels filled with water and oil are utilized with the force balance (top). Shown is the location of the motor and propellers that produce a constant flow. Wind tunnel schematic (bottom) illustrates set up for the wake traverse method. As air flows through the wind tunnel, the wake traverse lowers at a specified rate to measure the wake profile. Shown also is the infrared camera position utilized to visualize turbulence on the airfoil.

Military aircraft commonly experience transonic and supersonic flight, however commercial aircraft usually cruise between Mach 0.78 and 0.9.[102–103,105] In the lab, achieving transonic or

Materials
Views
www.MaterialsViews.com

ADVANCED
FUNCTIONAL
MATERIALS
www.afm-journal.de

Conventional airfoil side views and characteristics

Air flow

Thin wing section for low drag and high speed.
Suitable for race planes, fighters, interceptors, etc.

Thick wing section for high lift and low speed.
Suitable for wind turbines, transports, freighters, bombers, etc.

Curved thin wing section for high lift and low speed.
Suitable for transports, freighters, bombers, etc.

Reflex trailing edge wing section for low lift and high drag.
Suitable for good stability

Symmetrical wing section for low lift and high drag.
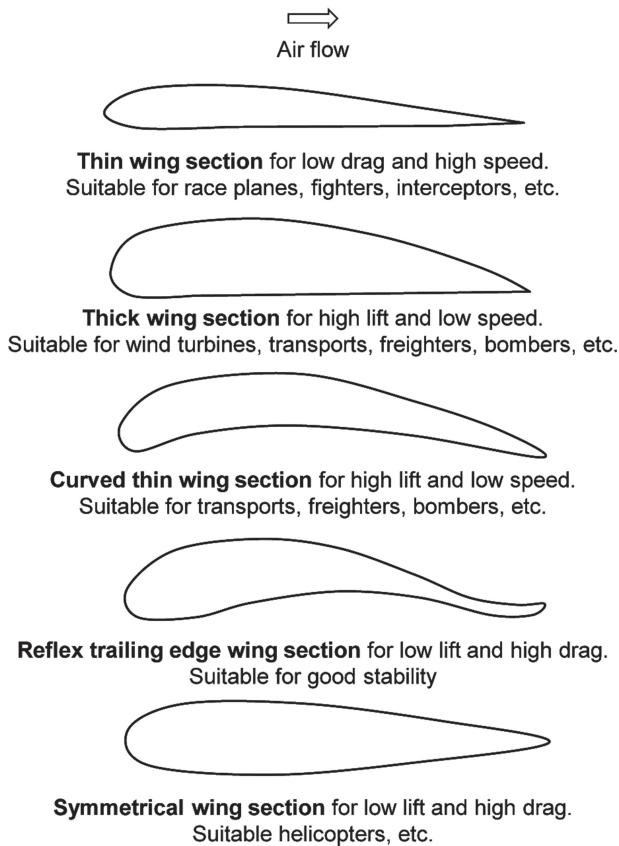Suitable helicopters, etc.

Figure 7. Conventional airfoil cross sectional side views. Shown are the thin, thick, curved thin, reflex trailing edge, and symmetrical wind sections. Each airfoil is designed for specific applications due to their various attributes such as low drag and high lift. Adapted with permission.[104]

supersonic flow requires specialized wind tunnels that are relatively expensive to operate. The airfoil angle of attack is shown in Figure 5, which is the angle between the level horizontal and the chord lines. This angle varies during flight in order to maintain lift, where at lower and higher speeds, a higher and lower angle of attack are required, respectively. Experiments have been conducted between 0° and 12° angle of attack in order to cover the majority of cruise conditions.[103,105]

Evaluating each of the airfoil designs over a wide range of Reynolds numbers covers a variety of applications of interest. For example, the wind turbine blades rotate much slower than the helicopter blade, so therefore lower Mach numbers and Reynolds numbers are applicable. Furthermore, various studies have examined complete or partial coverings of riblets on airfoils. Knowing that riblets may increase drag in laminar flow, riblets are only applied in the turbulent region of an airfoil, therefore leading to improved drag reduction. Trip strips are installed in many experiments in order to force transition to turbulence at a particular location.[102,103] A summary of conditions for open channel flat plate experiments is shown in Table 1 outlining the various riblet geometries, configurations, and materials that have been evaluated. Also Table 3 shows

wind tunnel experiments that have been conducted with various airfoils, conditions, riblet coverage, and trip strip locations.

3.3.2. Closed Channel

Measuring drag in closed channel flow is conducted with water, oil, and air experiments using both circular and rectangular cross section pipes and channels. Various closed channel experiments have been conducted using riblets applied to their interiors. In such cases, the fluid flows through the sample test area and the pressure difference between two points is measured with a pressure manometer, where lower pressure drop is desired. Apparatuses for both split round pipe and rectangular channel designs are illustrated in **Figure 8**a. Drag reduction is presented as negative $\Delta\tau/\tau_o$ (%) as well as pressure drop versus Reynolds

Methods (a) and apparatuses (b) to measure closed channel drag with water, oil, and air

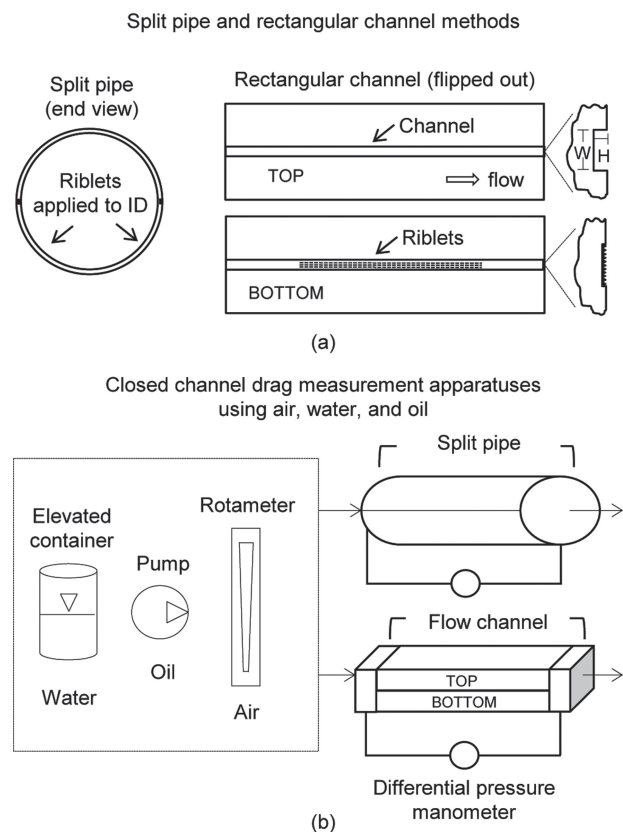Split pipe and rectangular channel methods

Figure 8. Closed channel methods and apparatuses to measure drag using water, oil, and air. a) Split designs are necessary in order to apply riblets inside micro-sized closed channels. Left schematic shows a round split pipe whilst the right shows a rectangular channel sandwich design. The rectangular channel allows for riblets to be fabricated on a flat surface, which may be desirable. Adapted with permission.[67] Copyright 2013, Elsevier. b) Drag is determined via pressure drop reduction using closed channels lined with riblet samples. Flow is regulated with the elevated container (water), pump (water or oil), and laboratory air connected to a rotameter (air). The pressure drop is measured with a manometer connected to both ends of the flow channel. Interface views are shown highlighting the top and bottom halves that are sandwiched together.

numbers. Drag reduction is also described with negative $\Delta P/P_o$ (%) values, where ΔP is the difference in pressure drop between the riblet sample (P) and the smooth (P_o) surfaces.

Generally the greatest challenge is applying riblets inside of the closed channel. For larger pipes (or macrosized closed channels), flexible sheets such as the 3M vinyl adhesive backed riblets can be applied to the interiors. Smaller pipes (or microsized closed channels) must be split in order to apply the flexible 3M riblet sheets. However, when riblets are not in the form of flexible sheets, they need to be fabricated via processes such as milling, soft lithography, or laser etching. Such fabrication generally requires flat and not curved surfaces. In these cases, the split rectangular channel design is more feasible by allowing riblets to be applied inside the channel prior to final assembly.

During experiments, fluid is introduced a variety of different methods depending on its viscosity and desired flow rates, as shown in Figure 8b. For instance, experiments with water have been conducted with both elevated bottle apparatuses[66,67] as well as syringe and gear pumps.[66–68,89] Experiments have been conducted with air flow by connecting a rotometer to a laboratory air supply,[66,67] in order to achieve particular flow velocities. In the case of water and oil experiments, flow velocity can be calculated from the volumetric flow rate and channel cross sectional area. A summary of experimental closed channel conditions is shown in Table 2 outlining the various riblet geometries, configurations, and materials that have been evaluated.

4. Riblet Results and Discussion

In this section, we present open followed by closed channel drag measurement results using water, oil, and air flow. Results are discussed and compared between the various measurement techniques, riblet geometries, riblet configurations, and flow regimes. This comparison helps to provide an overview understanding of the past and present work on riblet drag reduction.

Open and closed channel results can be presented similarly, including drag compared to riblet dimensions and aspect ratios. Comparing and studying such parameters allows for the development of lessons learned in order to optimize riblets. Microsized closed channel results are presented with pressure drop reduction compared to Reynolds number based on the channel dimensions. This differs from open channel results in order to account for hydraulic diameter, due to the interaction of vortices from neighboring walls, as described in Section 4.3. Therefore both open and closed channel results are presented in forms that best represent their findings.

4.1. Open Channel

In open channel flow using water, oil, and air, results indicate that properly designed riblets can reduce drag. A summary of experimental results are presented in Table 1 for flat plate and Table 3 for wind tunnel airfoil flow. Several studies have included varying geometries and configurations, which have been conducted with laminar through turbulent flow. Drag
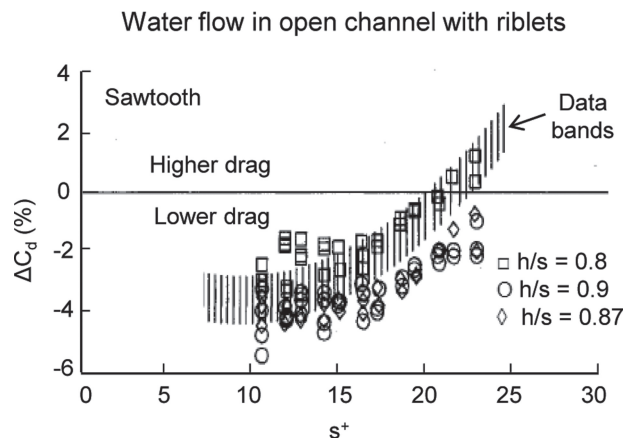

Figure 9. Open channel experimental results with riblets in water flow. Drag reduction is presented as Reynolds numbers compared to negative ΔC_d (%) values, which is the percentage drag coefficient reduction between the smooth and riblet samples. Riblet samples with various h/s values are compared, with the maximum drag reduction near 6%. Riblets are sawtooth geometry and continuous configuration. Adapted with permission.[49] Copyright 1990, American Institute of Aeronautics and Astronautics.

reduction is presented as negative $\Delta \tau/\tau_o$ (%) and ΔC_d (%) values compared to Reynolds numbers.

4.1.1. Flat Plate Experiments

Water channel experiments indicate maximum drag reduction of nearly 6% using continuous sawtooth riblets on a flat plate, as shown in **Figure 9**. Results also show that the greatest drag reduction is around s^+ equaling 10–15,[80] which correlates well with oil channel findings.[52] Extensive research has been conducted with oil channel flow, since oil allows for larger scale riblets, which drastically eases the challenge of riblet fabrication. Such experiments include blade, sawtooth, and scalloped riblet geometries with continuous and staggered segmented configuration, all using white paraffin oil ($\nu = 1.2 \times 10^5$ m²/s). This research is highlighted in **Figure 10**a, showing a wide range of h/s values, which are deemed important in determining the optimal drag reducing geometry. A summary of oil channel experiments is provided in Figure 10b, showing the greatest drag reduction from each of the geometries.[52] Furthermore Figure 10c shows the effect of continuous and staggered segmented configurations.[52,53]

Results indicate maximum drag reduction of nearly 9% is possible with blade riblets where $h/s = 0.5$, $t/s = 0.04$, and $s^+ \approx 15$. This drag reduction further improves with a lower t/s value of 0.02, where maximum drag reduction is nearly 10%.[52] Furthermore, sawtooth riblets with $h/s = 0.98$ and $\alpha = 54°$ provides the greatest drag reduction of nearly 6%, indicating that the smaller α is beneficial. Also scalloped riblets with $h/s = 0.7$ provides the greatest drag reduction of nearly 7%. Results also indicate that staggered segmented trapezoidal shaped riblets provided less drag reduction compared to continuous blade riblets (about 6% versus 10%).[52,53] However, the staggered segmented provides drag reduction (albeit less magnitude) for a larger s^+ range, as compared to the continuous riblets.

www.MaterialsViews.com

**ADVANCED
FUNCTIONAL
MATERIALS**
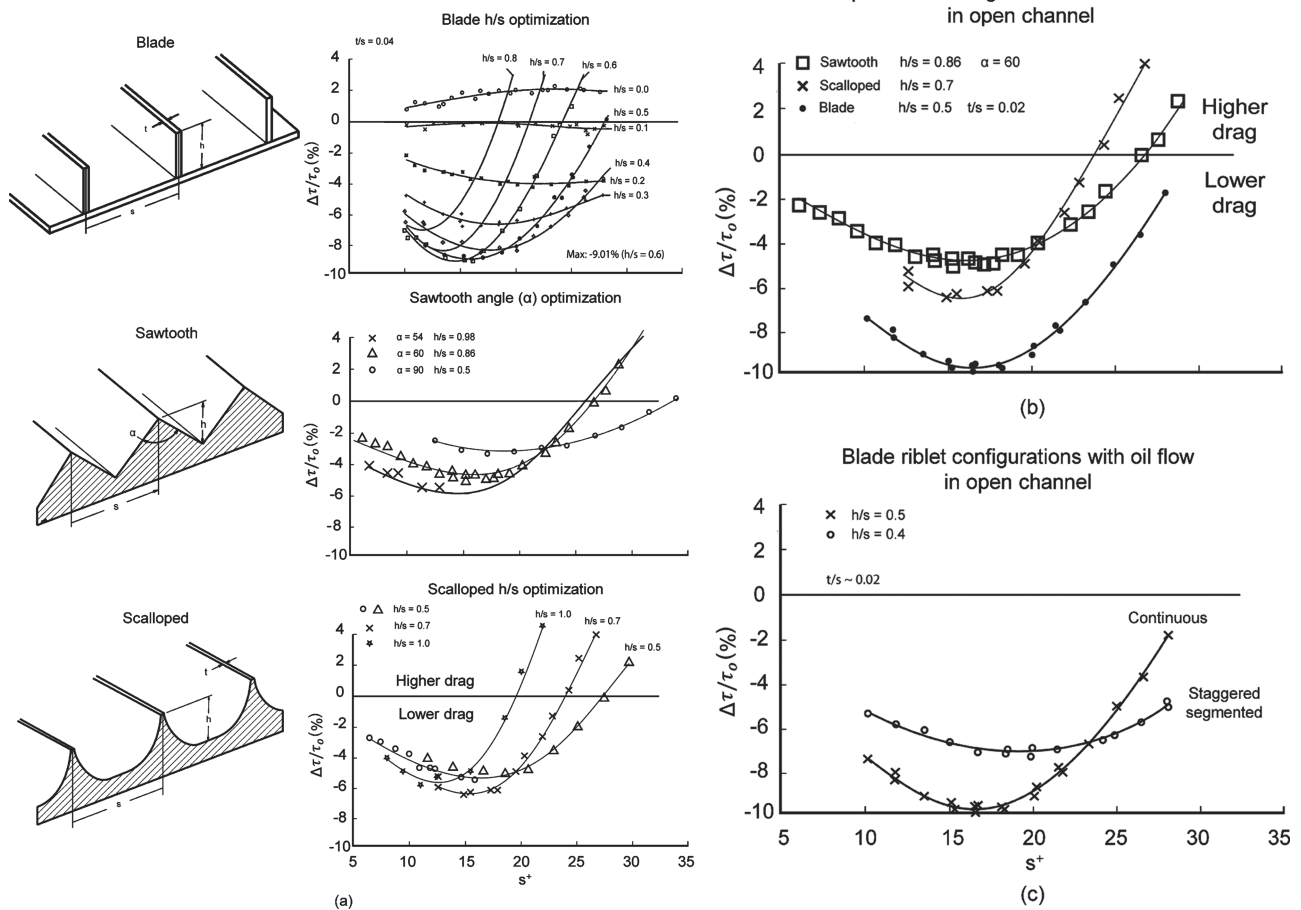www.afm-journal.de

FEATURE ARTICLE

Figure 10. Open channel experimental results with riblets in oil flow. Drag reduction is presented as Reynolds numbers compared to negative $\Delta\tau/\tau_o$ (%) values, where $\Delta\tau$ is the difference between shear stresses on the riblet sample (τ) and the smooth (τ_o) surfaces. a) Various experiments with blade, sawtooth, and scalloped riblets were conducted in order to discover the optimal geometry for maximum drag reduction. Varied parameters include the riblet geometry, h/s, t/s, and s^+, which allows for a better comparison between experiments. Oil channel experiments were conducted using white paraffin oil. b) Maximum drag reduction results from the various blade, sawtooth, and scalloped experiments are compiled. Results indicate that the blade geometry with $h/s \approx 0.5$ and $t/s \approx 0.02$ produces the maximum drag reduction of 10% near $s^+ \approx 15$. Panels (a,b) adapted with permission.[52] Copyright 1997, Cambridge University press. c) Experimental results comparing continuous and staggered segmented blade riblets, indicating that latter configuration shows less drag reduction. Adapted with permission.[52,53] Copyright 1997, Cambridge University Press and copyright 2000, Springer.

4.1.2. Flat Plate Observations

Many observations can be made from studying the presented water and oil channel experimental results. For instance, riblets with lower h/s values show less maximum drag reduction but over a wider range of s^+ values (e.g., blade riblets where $h/s = 0.2$–0.3 versus $h/s = 0.5$). This is presumably due to the vortices interacting with larger area on the riblets and with each other. Previously presented flow visualization indicates for the higher flow velocity (where s^+ and h^+ increase and $h/s = 0.5$) the vortices appear to lower in vertical elevation, and shear stresses at the riblet tips are believed to increase. With constant h and increasing s values (thus lowering h/s), it is believed that the vortices lower in between the riblets (for instance at $h/s = 0.2$–0.3 versus $h/s = 0.5$). Furthermore, increasing h/s increases wetted surface area between riblets, which leads to increased friction and thus drag.

Choosing an optimal h/s based on the aforementioned experimental results depends on particular applications, specifically whether or not the flow velocities are known or constant. For instance, riblets may be optimized for drag reduction over a wider range of s^+ values, where flow velocity conditions are varying. Conversely, riblets may be optimized for maximum drag reduction over a smaller s^+ range, where flow velocity is relatively constant, such as aircraft at cruising speed. In addition to h/s, the t/s ratio affects drag, where the smaller ratio is desirable. Furthermore research suggests that drag reduction is possible with sawtooth and scalloped riblets, but such geometries require differing h/s values. It should be noted that the blade riblets are the most fragile, followed by scalloped and sawtooth, so therefore clear tradeoffs are necessary when designing riblets for commercial applications.
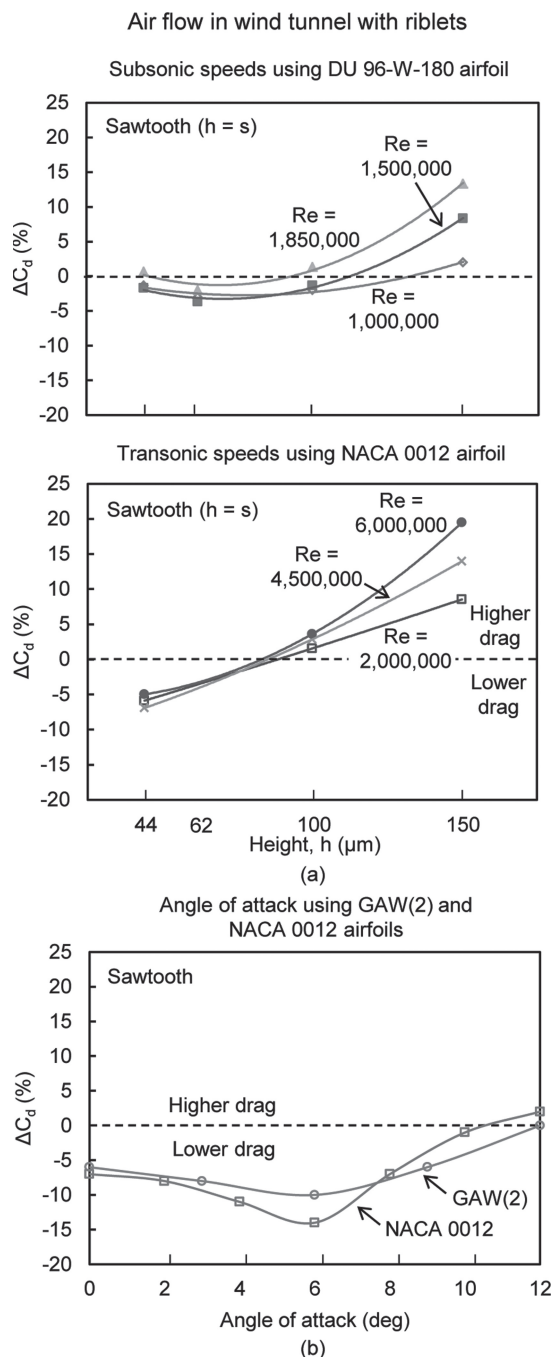
Air flow in wind tunnel with riblets

Subsonic speeds using DU 96-W-180 airfoil

Transonic speeds using NACA 0012 airfoil

Angle of attack using GAW(2) and NACA 0012 airfoils

Figure 11. Wind tunnel experimental results with riblets on airfoils. Drag reduction is presented as Reynolds numbers compared to negative ΔC_d (%) values, which is the percentage drag coefficient reduction between the smooth and riblet samples. a) Drag reduction is shown with wind turbine DU 96-W-180 (adapted with permission.[64] Copyright 2011, American Institute of Aeronautics and Astronautics) and symmetrical NACA 0012 (present work) airfoils with various 3M Corp. sawtooth riblets. The top and bottom figures show Reynolds numbers in the subsonic and transonic ranges, respectively. Maximum drag reduction is near 7% for the riblets with $h = s = 44$ μm in transonic flow. b) Riblet drag reduction is related to angle of attack, as shown with two airfoils with angles of attack up to 12°. The greatest drag reduction of nearly 14% is shown at 6° angle of attack. Adapted with permission.[60] Copyright 1999, American Institute of Aeronautics and Astronautics.

4.1.3. Airfoil Experiments

With the advent of the 3M vinyl riblet sheets, many experiments have been conducted with airfoils in wind tunnels. Such experimental results are shown in **Figure 11**a for riblets applied to the wind turbine DU 96-W-180 airfoil as well as the aircraft wing NACA 0012 airfoil. Results indicate that the smaller height riblets provide the greatest drag reduction, around 2% for the DU 96-W-180 airfoil[64] and 7% for the NACA 0012 airfoil (present work). Larger sized riblets and higher Reynolds numbers provide less drag reduction, and in some cases the drag increases compared to the smooth airfoil. The Reynolds numbers for experiments provide a wide spectrum of subsonic (Ma <.75 with $Re = 1\,000\,000$) to transonic (0.75 < Ma < 1.2 with $Re = 6\,000\,000$) velocities. This allows for comparison airfoils, Reynolds numbers, and riblet sizes. An additional variable of interest includes the angle of attack, as shown in Figure 11b using sawtooth riblets. The greatest drag reduction nearly 14% occurs at 6° angle of attack for the NACA 0012 airfoil.[60]

Since riblets are more effective in turbulent versus laminar regimes, and in order to better compare experiments, it is important to understand which areas of the airfoil are experiencing turbulence. Images in **Figure 12** (present work) were taken during transonic wind tunnel NACA 0012 airfoil experimentation with a total covering from leading to trailing edges of vinyl sawtooth riblets provided by 3M Corp. The infrared camera detects heat generated by skin friction on the airfoil surface due to the turbulent boundary layer, where lighter colors indicate higher temperatures. As illustrated, a turbulent trip
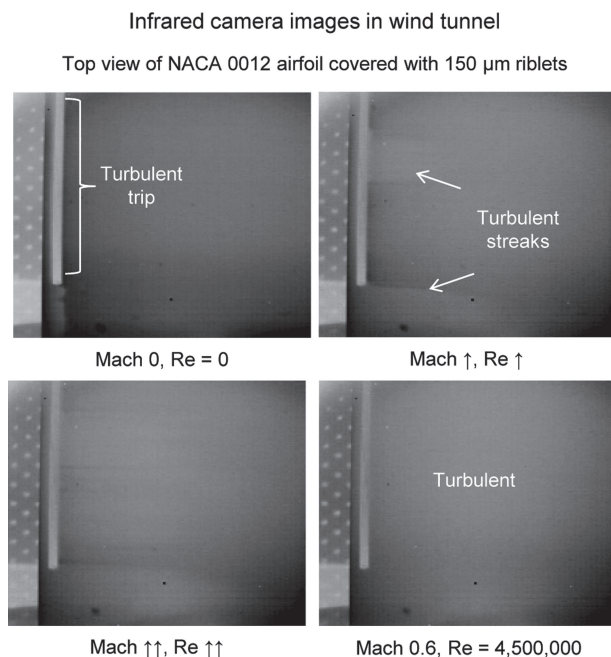
Infrared camera images in wind tunnel

Top view of NACA 0012 airfoil covered with 150 μm riblets

Figure 12. Detecting turbulent air flow using an infrared camera (present work). In order to determine the extent of turbulent flow on an airfoil, an infrared camera may be employed. The friction from turbulent vortices heats the airfoil surface and is detected by the camera. Based on the airfoil geometry and calculated air velocity using pressure taps measurements, a fully turbulent state is shown with Mach 0.6 and $Re = 4\,500\,000$.

www.MaterialsViews.com

ADVANCED
FUNCTIONAL
MATERIALS
www.afm-journal.de

FEATURE ARTICLE

strip is installed on the leading edge in order to ensure turbulent flow. Detecting the increased heat with an infrared camera is normally conducted with polymer airfoils, since the heat generated remains on the surface. However the airfoil utilized in the experiments was metallic, which acted as a heat sink, thus having the potential of lowering the surface temperature. Nevertheless, it was found that the vinyl sawtooth riblets applied to the metallic airfoil provided sufficient insulation from the heat sink effect thus providing usable images. Reynolds number is calculated from airfoil geometry and the wind speed found from pressure tap measurements.[106]

The images in Figure 12 are shown from the start to the end of experimentation (0 < Mach < 0.6 and 0 < Re < 4 500 000), with the white streaks representing turbulence. The upper left image shows the beginning state before experiments, indicating the baseline airfoil surface temperature based on ambient air temperature conditions. The upper right image shows that with increasing Mach and Reynolds numbers that turbulent white streaks begin to appear. The bottom left image shows that with higher Mach and Reynolds numbers that the white streaks cover more of the airfoil surface. Finally, the bottom right image shows what is believed to be a fully turbulent state with white streaks covering nearly the entire airfoil surface. As indicated earlier a Reynolds number over 500 000 for open channel flat plate flow is considered turbulent, and the Reynolds number here is calculated at 4 500 000.

Boundary layers shown in **Figure 13** illustrate a conceptual model of flow over an airfoil and flat plate. As shown with increasing Mach number (and thus Reynolds number), the turbulent boundary layer thickness decreases. Riblets are effective by remaining inside the turbulent viscous sublayer, in order to

properly lift and presumably pin any vortices. However, if the riblet protrudes outside of the viscous sublayer, the increased surface area of the riblets will increase skin friction and thus drag. Therefore, it is believed that riblets must remain within the viscous sublayer in order to provide benefit.

4.2. Closed Channel

In closed channel flow using water, oil, and air, results indicate that properly designed riblets can reduce drag. A summary of microsized closed channel experimental results are presented in Table 2. Several studies have included varying geometries and configurations, which have been conducted with laminar through turbulent flow. Drag reduction is presented as negative $\Delta\tau/\tau_o$ (%) and pressure drop values compared to Reynolds numbers.

4.2.1. The Role of Channel Dimensions

A comparison of open and macro-sized closed channel results show that drag reduction is similar when neighboring wall effects are negligible, as indicated in **Figure 14**. These results represent cases when neighboring walls are sufficiently far apart, as shown with pipe diameters approximately 25 mm or greater. However when channel dimensions are relatively small (as shown in Figure 8a with microsized closed channel where $H = 0.7$ mm and $W = 3.2$ mm), neighboring wall effects are believed to play an important role in riblet drag reduction. A set of experiments were conducted with such microsized closed channels, with results presented in the following section.

4.2.2. Microsized Channel Experiments

Microsized closed channel experiments have included varying geometries, configurations, hydrophobicity, oleophilicity, and channel dimensions with laminar through turbulent flow.[67–68] The presented results include samples reported with riblets designated as "sample description (h/s, t/s)" value. For example, the 3M riblet sample with height and spacing equaling 44 µm is written as "44 µm (1, 1)" or more simply "44 µm sample". The baseline blade dimensions were $h = 127$ µm, $vw = 280$ µm, and $t = 127$ µm, with variations presented later in the modeling section. All samples exhibit blade geometry with the aligned segmented configuration, except the 3M riblets which exhibit sawtooth geometry and continuous configuration. Also select riblet samples received a nanostructured coating (e.g., "coated" samples). Such coated samples are either superhydrophobic or superoleophilic, and are believed to improve riblet smoothness. Furthermore, the same nanostructured coating applied to replica shark skin samples indicates that the coating lowers adhesion forces.[24]

Presented are microsized closed channel water and air results in **Figure 15** and oil (white paraffin oil with CAS 8012-95-1) in **Figure 16**, which are compared to the flat milled sample. Various riblet geometries and dimensions were evaluated in flows ranging from laminar to turbulent regimes. The effect of h/s and t/s, h, hydrophobicity/oleophilicity, and smoothness are

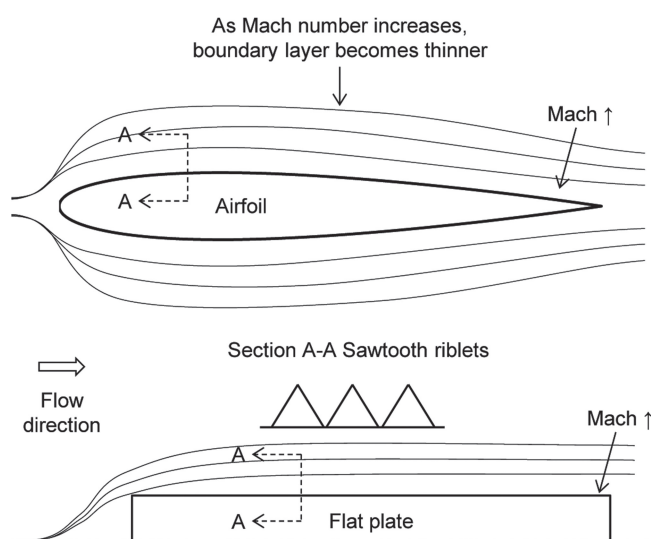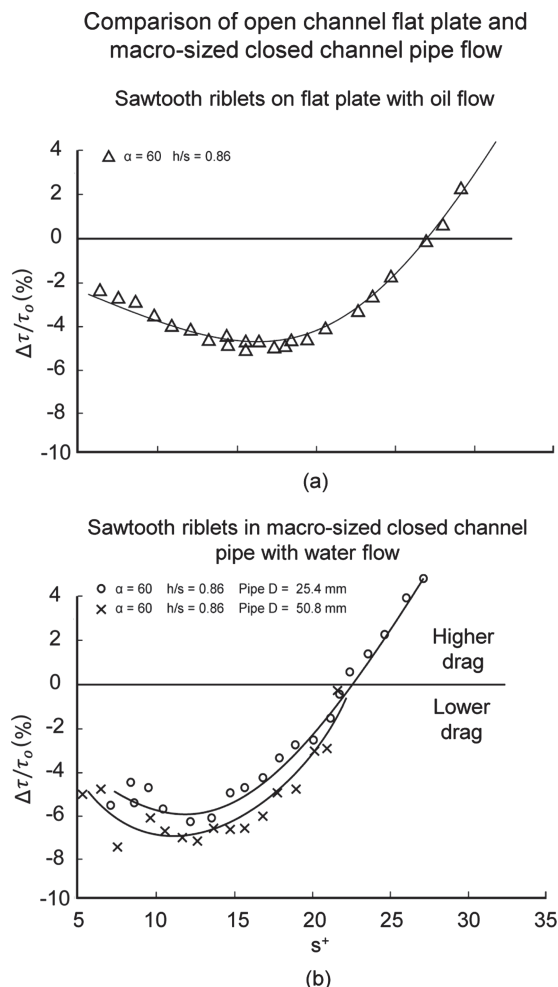## Boundary layer thickness related to riblet height (not to scale)

Figure 13. Boundary layer thickness related to riblet height. As the Mach number increases, the boundary layer thickness decreases. It is believed for drag reduction that riblets should remain inside the viscous sublayer in order to effectively control the turbulent vortices. Shown is an illustration (not to scale) explaining the relationship.

FEATURE ARTICLE

Comparison of open channel flat plate and macro-sized closed channel pipe flow

Sawtooth riblets on flat plate with oil flow

△ α = 60   h/s = 0.86

(a)

Sawtooth riblets in macro-sized closed channel pipe with water flow

○ α = 60   h/s = 0.86   Pipe D = 25.4 mm
× α = 60   h/s = 0.86   Pipe D = 50.8 mm

Higher drag

Lower drag

(b)

Figure 14. Comparison of open channel flat plate and macrosized closed channel pipe flow (where neighboring wall effects are assumed negligible). Drag reduction is presented as Reynolds numbers compared to negative $\Delta\tau/\tau_o$ (%) values, where $\Delta\tau$ is the difference between shear stresses on the riblet sample (τ) and the smooth (τ_o) surfaces. Samples consist of sawtooth geometry where the angle $\alpha = 60°$, as defined in Figure 10a. a) Experimental results are shown with sawtooth riblets on a flat plate and b) in round pipe with diameter D. Maximum drag reduction is similar between the presented flat plate and macrosized pipe flow. Panel (a) reproduced with permission.[52] Copyright 1997, Cambridge University Press. Panel (b) reproduced with permission.[65] Copyright 1990, American Institute of Aeronautics and Astronautics.

shown. The shallow sample shows the most pressure drop reduction at 19% in water and 13% in air.[67] Due to their initial performance, these riblets received the nanostructured coating, which then produced an improved pressure drop reduction of 34% in water and 24% in air.[67] The 100 μm sample also reduced pressure drop by 30% in water. In oil flow, the narrow sample shows the most pressure drop reduction at 9%.[68]

4.2.3. Microsized Channel Observations

Many observations can be made from studying the presented water, oil, and air microsized closed channel experimental

results. For instance, lower h/s values appear to provide the greatest drag reduction, although this differs from the open channel results. However with rectangular microsized closed channel experiments, the neighboring wall effects are believed to play a role in the drag reduction. In the closed channel experiments, samples with the lowest h/s performed the best presumably due to less interaction between the vortices on the top and the bottom. This effect is described later in more detail.

Understanding the differences in performance between riblet samples in water, oil, and air flow can be explained by considering the Reynolds numbers as well as the drag reducing mechanisms. It is believed that different mechanisms are at work, mainly due to the effect of viscosity, as well as Reynolds number. For instance, water and air flow was turbulent, where the riblets are believed to lift and pin the vortices, and thus reduce drag. However, oil was laminar, which benefited from the so-called thin oil film, which reduces skin friction at the solid–liquid interface and thus reduces drag.[68] The thin oil film effect will be shown and discussed later in more detail. Additionally, it is believed that turbulent oil flow would benefit from the shark skin effect.

4.2.4. Continuous Versus Segmented Riblets

To understand the effects of riblet configurations, namely continuous and aligned segmented, a series of water, oil, and air flow experiments were conducted.[67–68] Results are presented in **Figure 17**, which shows the blade samples Continuous and Baseline, representing the continuous and aligned segmented configurations respectively. Intuitively, the Continuous sample should provide higher drag due to the increased wetted surface area. Each experiment with the Continuous sample exhibits a higher drag as compared to the Segmented sample. However, this drag increase is less with air as compared to water, for similar Reynolds numbers. The continuous blades may reduce cross stream movement with air more efficiently than with segmented blades. As the lower viscosity air vortices rotate in the channel, the gap area between segmented blades perhaps disrupts and unpins the vortices.

4.2.5. Riblets on Top or Bottom or Both Sides

To understand the effects of riblets on one versus two sides and with differing microsized channel heights, a series of water flow experiments were conducted.[67] Such combinations included experiments with 1× channel height, 2× channel height, riblets on bottom, riblets on top, and riblets on top and bottom; all with Shallow samples. The top row of **Figure 18** shows results from riblets on the top only and bottom only. Results indicate that riblets located on the bottom side perform differently from the same riblets located on the top side. The pressure drop increases by 20% when the riblets are transferred from the bottom to the top.[67]

Similar experiments were conducted to study the effect of channel height with riblets on the top or bottom. Results indicate that pressure drop with the riblets on the bottom are unaffected by channel height, but pressure drop improves with topside riblets and 2× channel height. The bottom row

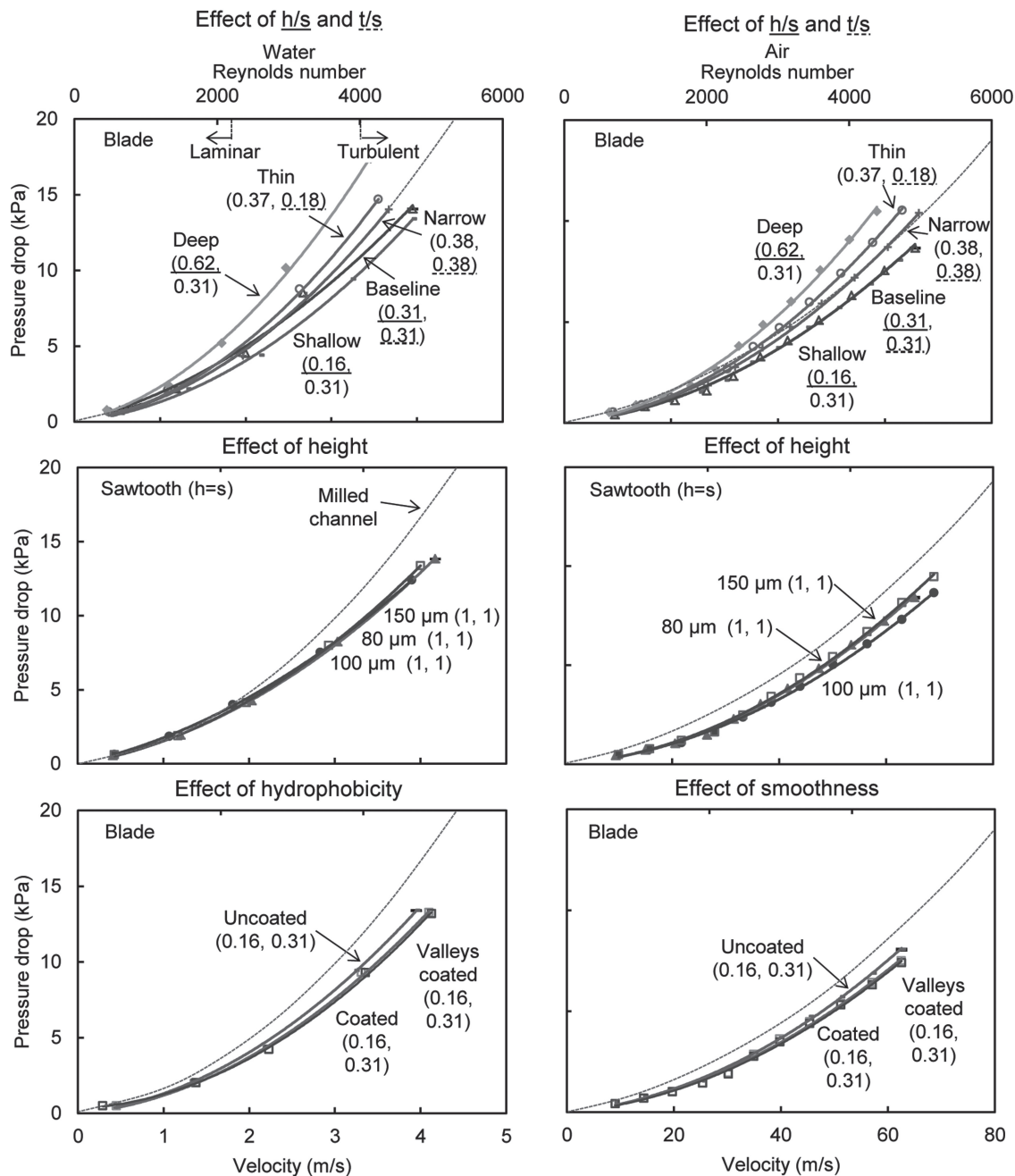**Water and air flow in micro-sized closed channel with riblets**

Figure 15. Microsized closed channel experimental results with riblets in water and air flow. Drag reduction is presented as Reynolds numbers compared to pressure drops between the inlet and outlet of the channel, where lower pressure drop is desirable. Riblets of varying geometries were evaluated in laminar ($Re < 2300$) through turbulent flow ($Re > 4000$) conditions. Experiments evaluated the effect of h/s, t/s, height, hydrophobicity, and smoothness. Riblets were fabricated via laser etching, and a nanostructured coating was applied to achieve the desired hydrophobicity and smoothness. Maximum pressure drop reduction of 34% with water was recorded for hydrophobic riblets in the turbulent regime. Flat milled channel control sample is shown for comparison. Error bars show ±1 standard deviation. Adapted with permission.[67] Copyright 2013, Elsevier.

of Figure 18 shows results from riblets on both the top and bottom sides of the channel. Neighboring wall effects are assumed by observing the percentage pressure drop with the 1× channel height and decrease with the 2× channel height. It is believed that the vortices from neighboring walls with the

1× channel height interact and increase the drag, but the larger gap distance in the 2× channel height reduces this effect. The aforementioned effects are believed to have a connection with the vortices interaction, as described later when presenting the conceptual models.

ADVANCED
FUNCTIONAL
MATERIALS
www.afm-journal.de

Materials
Views
www.MaterialsViews.com

Oil flow in micro-sized closed channel with riblets

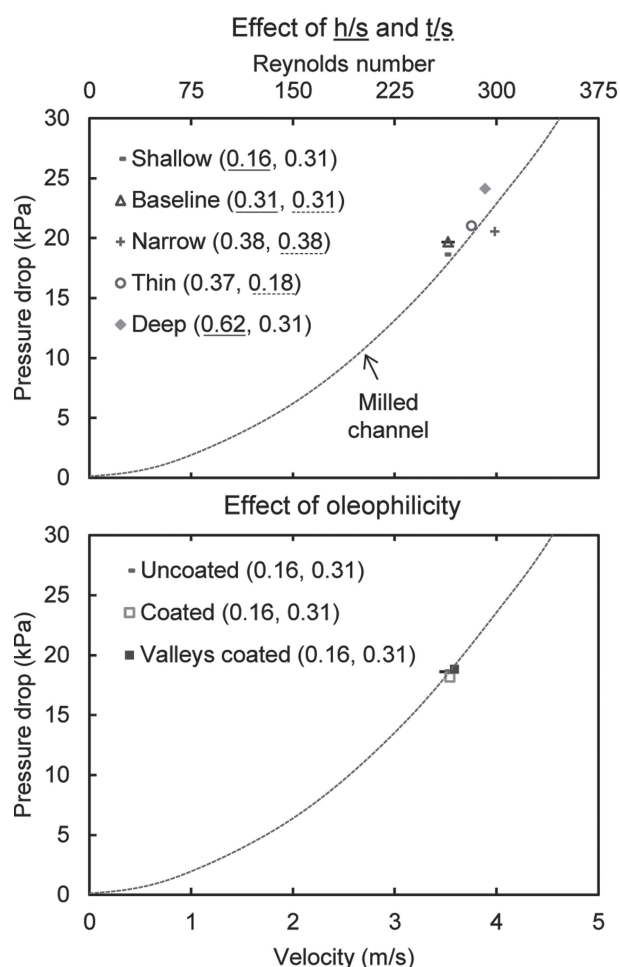## Effect of continuous vs. segmented riblets with micro-sized closed channel flow

Figure 16. Microsized closed channel experimental results with riblets in oil flow. Drag reduction is presented as Reynolds numbers compared to pressure drops between the inlet and outlet of the channel, where lower pressure drop is desirable. Riblets of varying geometries were evaluated in laminar ($Re < 375$) flow conditions. Experiments evaluated the effect of h/s, t/s, and oleophilicity. Riblets were fabricated via laser etching, and a nanostructured coating was applied to achieve the desired oleophilicity. Maximum pressure drop reduction of 9% was recorded for the Narrow riblets. Experiments were conducted using white paraffin oil. Flat milled channel control sample is shown for comparison. Error bars show ±1 standard deviation. Adapted with permission.[68] Copyright 2013, Royal Society of Chemistry.

4.2.6. The Role of Riblet Wettability

A correlation exists when comparing riblet sample pressure drop results with and without the nanostructured coating. It was discovered that only appropriately sized riblets coupled with the nanostructured coating provide drag reducing benefit. Contact angle measurements in air using water and white paraffin oil droplets (5 µL) for the various samples are shown in **Figure 19**.[67,68] In water flow, drag reduction improves with superhydrophobicity and low adhesion,[24,67] in air flow with smoothness,[67] and in oil flow with superoleophilicity.[68] Results indicate that the coupling of appropriately sized
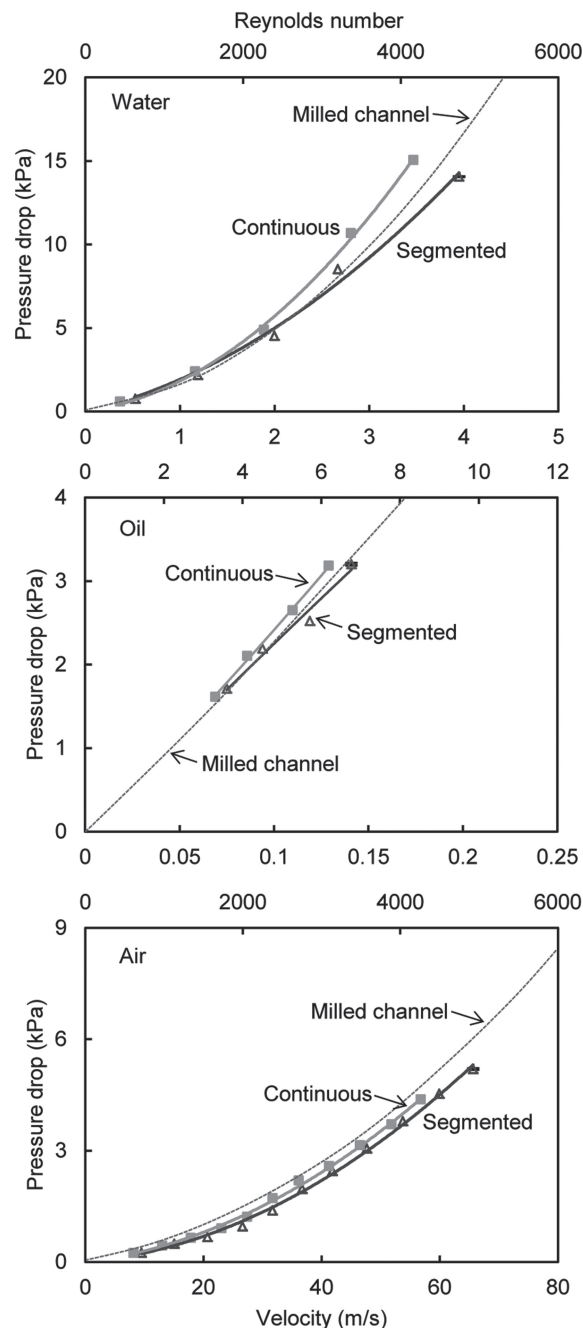
Figure 17. Microsized closed channel experimental results showing the effect of continuous vs. segmented blade riblets with water, oil, and air flow. Drag reduction is presented as Reynolds numbers compared to pressure drops between the inlet and outlet of the channel, where lower pressure drop is desirable. Riblets were evaluated in laminar ($Re < 2300$) through turbulent flow ($Re > 4000$) conditions. Results indicate that the continuous riblets increase drag with all fluids, presumably due to the increased wetted surface area, which leads to higher skin friction. Flat milled channel control sample is shown for comparison. Error bars show ±1 standard deviation. Adapted with permission (water/air (top and bottom panels),[67] Copyright 2013, Elsevier) and (oil (middle pannel),[68] Copyright 2013, Royal Society of Chemistry).
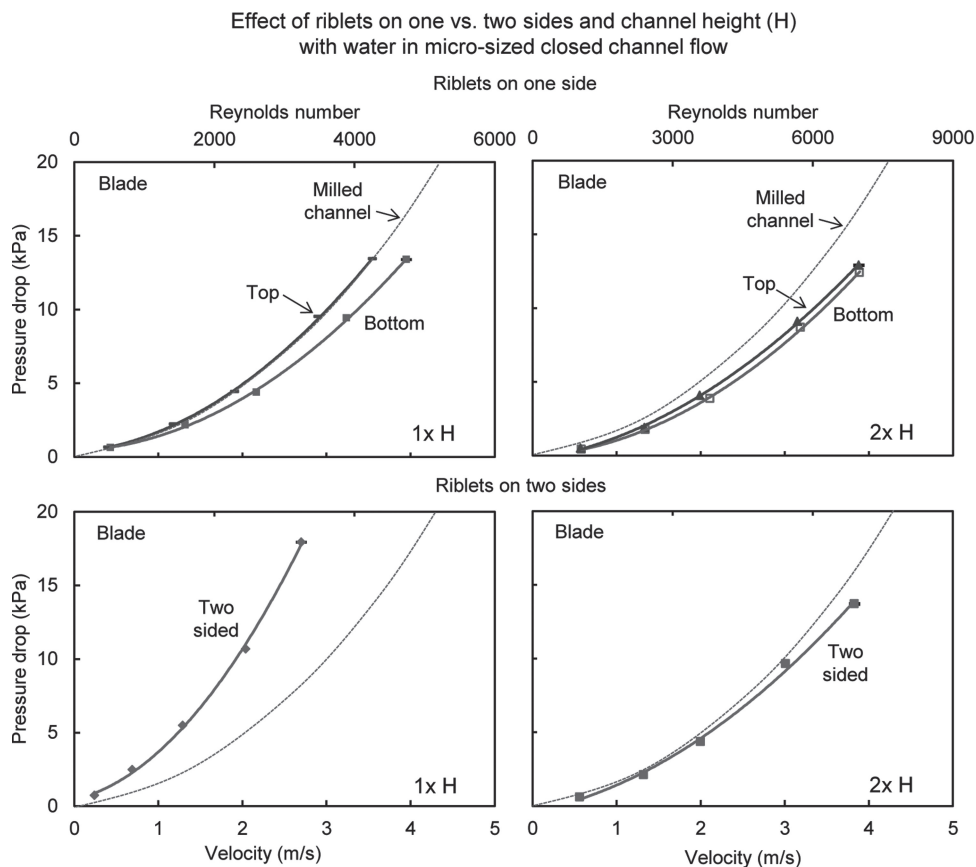
Figure 18. Microsized closed channel experimental results showing the effect of channel height and riblets on the top, bottom, or both sides with water flow. Drag reduction is presented as Reynolds numbers compared to pressure drops between the inlet and outlet of the channel, where lower pressure drop is desirable. Riblets were evaluated in laminar ($Re < 2300$) through turbulent flow ($Re > 4000$) conditions. Results indicate that riblets on the bottom reduce drag more than when positioned on the top of the channel. Also, 2× channel height reduces drag, presumably due to vortices from the top and bottom moving apart (i.e., neighboring wall effects are negligible). Flat milled channel control sample is shown for comparison. Error bars show ±1 standard deviation. Adapted with permission.[67] Copyright 2013, Elsevier.

riblets with the nanostructured coating is necessary. For instance, shark skin replicas were examined in another study with the nanostructured coating, and the oil drag increased. This was likely due to the absence of the thin oil film effect.[68]

4.3. Models of Riblets and Vortices

Experimental results with open and closed channel flow indicate drag reduction for a variety of riblets in water, oil, and air flow. However design principles differ depending on microsized closed channel dimensions, due to neighboring wall interactions. For instance, results indicate h/s for maximum drag reduction should be 0.5 for open channel and 0.16 for microsized closed channel flow. In order to fully understand the mechanisms behind the drag reduction, careful consideration is given to the boundary layer and riblet interaction. With experimental data from both water and air, there are several theories to imagine when describing the behaviors of vortices in turbulent conditions. Also presented is the drag reduction theory for laminar oil flow, which is called the thin oil film effect.

4.3.1. Riblets for Open or Macrosized Closed Channel Flow

Illustrations shown in **Figure 20** provide one explanation of turbulent flow behavior and the effects of riblets of varying geometries, when neighboring wall effects are negligible.[67] Shown are the effects on drag with regards to riblet tip to vortices contact area, riblet valley wetted surface area, vortices entanglement, and vortices pinning. Dimensions of interest include h, s, t, and vw. The riblets and vortices are believed to be scalable; with the dominate features being lateral spacing (s^+), where s^+ equaling one third the vortex diameter is believed to provide maximum drag reduction with a variety of fluids and flow conditions. The s^+ value is an important parameter to study, since an s^+ too large allows vortices to drop between riblets, and an s^+ too small increases riblet tip to vortices contact area, both of which increase drag. In general, minimizing the higher velocity vortices' contact is desired, along with minimizing wetted perimeter for the lower velocity flow between riblets.[67]

Entanglement is perhaps worse with the flat plate, and is believed to occur when riblets are too closely spaced. As thickness

**ADVANCED
FUNCTIONAL
MATERIALS**

www.afm-journal.de

FEATURE ARTICLE
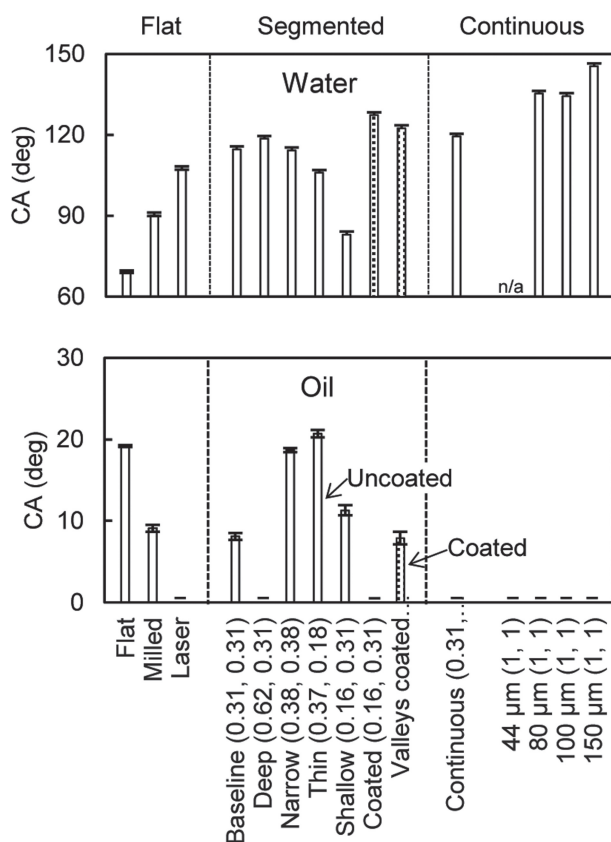
Materials Views

www.MaterialsViews.com

Figure 19. Apparent contact angle (CA) measurements for laser etched riblet samples; both with and without the nanostructured coating. Shown on the top and bottom are measurements at the solid-air-water (adapted with permission.[67] Copyright 2013, Elsevier) and solid-air-oil (adapted with permission.[68] Copyright 2013, Royal Society of Chemistry) interfaces, respectively. Error bars show ±1 standard deviation.
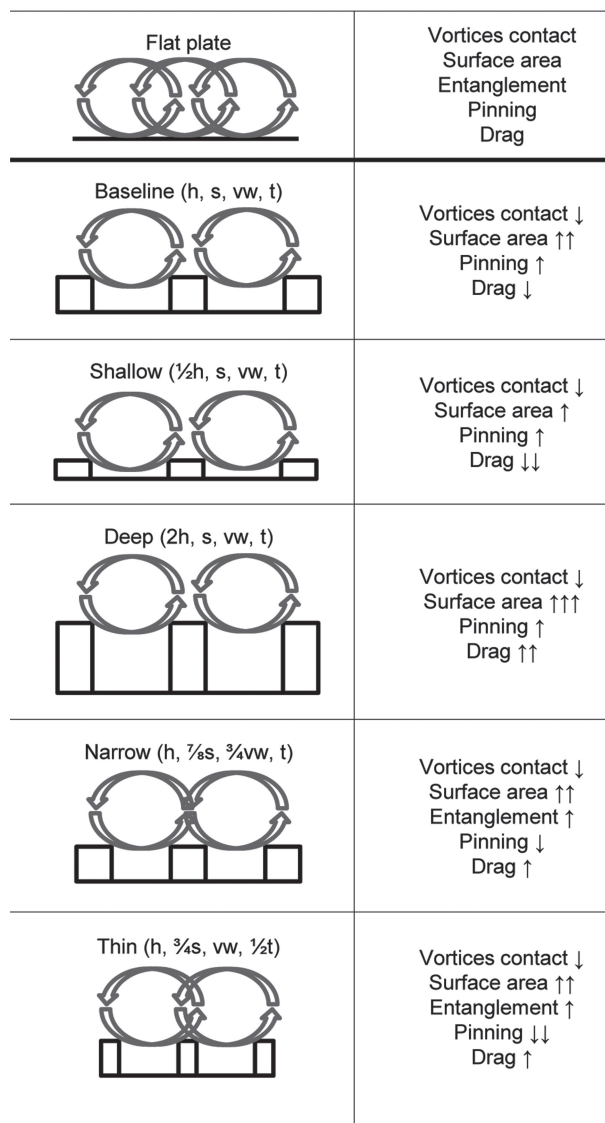

Figure 20. Scale conceptual models of turbulent vortices interacting with various riblet geometries. Drag reduction is believed to be possible by lifting and pinning the naturally occurring fluid vortices. This results in less shear stress, momentum transfer, and vortices ejection from the viscous sublayer. A minimum riblet height is necessary to lift and pin the vortices. Adapted with permission.[67] Copyright 2013, Elsevier.

increases, so does drag, which is due to higher contact area between riblet tips and vortices. Therefore a minimal thickness is desired, although thickness is determined by fabrication techniques and material properties to maintain structural integrity during flow. The height effect is evident when comparing the three riblet heights, since the Deep sample shows the highest drag likely due to its increased riblet valley wetted perimeter. The h/s ratios were varied with increasing or decreasing height, which also affects the wetted perimeter of the sample. The best performer is the Shallow sample, since it is believed that the vortices are still lifted and pinned, but the entanglement and wetted perimeter are minimized. Furthermore, the values of t and t/s should be minimized in order to reduce the contact with the higher speed vortices, which are believed to interact with riblet tips.[67]

4.3.2. Riblets in Microsized Closed Channel Flow

Micro-sized closed channel flow operates differently than macrosized closed channel or open channel flow, so therefore

an applicable conceptual model was developed as shown in **Figure 21**.[67] During such flow when neighboring wall effects play a role, vortices from the top and bottom perhaps mix and their rotation is either additive or subtractive. The illustration highlights the assumed interaction between the vortices in microsized closed channel flow with and without riblets. This model shows how the top and bottom vortices may interact, which was developed from microsized channel and flow visualization experimental data presented earlier. Illustrated are channels with flat surfaces, riblets only on the bottom, riblets only on the top, riblets on both sides, and riblets on both sides with

Materials
Views
www.MaterialsViews.com

ADVANCED
FUNCTIONAL
MATERIALS
www.afm-journal.de

FEATURE ARTICLE

Vortices interaction with riblets in micro-sized closed channel (flow into page, to relative scale)
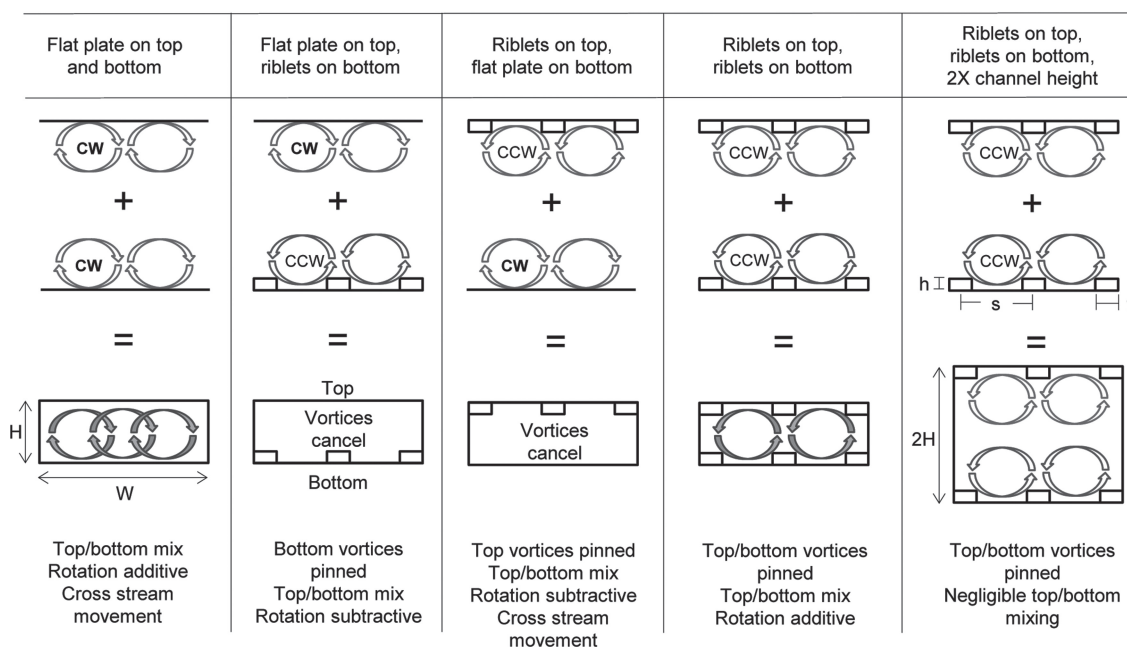

Figure 21. Scale conceptual models of microsized closed channel showing turbulent vortices' behaviors with the flat, Shallow sample, one or two sided, and 2× channel height combinations. Vortices are assumed to rotate clockwise on a flat plate and counterclockwise on riblets. When considering the two-sided nature of a closed channel, the rotational direction is believed to account for drag increase or reduction. A 1× channel height is believed to allow vortices from the top and bottom to interact and either increase the rotational speed or cancel each other. Cross stream movement occurs when vortices are not properly pinned, for instance as shown with a flat plate. Increasing the channel height to at least 3× vortex diameter is believed to move the top and bottom side vortices apart so that neighboring wall effects are negligible. Adapted with permission.[67] Copyright 2013, Elsevier.

a doubled height. Understanding these interactions will aid in the design of efficient microsized closed channel flow systems.

In these models, vortices seem to rotate clockwise on flat plates and counterclockwise on riblet surfaces. This difference in direction affects how the vortices mix by determining if they reduce or increase total drag. Vortices that rotate in opposite directions may cancel each other and reduce total drag, as shown with riblets on one side (top or bottom). When no riblets are present, the vortices are believed to mix from the top and bottom, as well as translate in the cross stream direction, thus leading to high drag. Conversely, vortices that rotate in the same direction may add to one another, and increase total drag. When considering riblets on both sides (2× channel height), the vortices are believed to be lifted and pinned as expected. Furthermore since the channel height is ample, the top and bottom do not mix, thus reducing drag. Therefore a channel height of at least 3× the diameter of vortices (or ≈150 wall units) is believed necessary to reduce drag.[67]

4.3.3. Thin Oil Film Effect

As previously mentioned, it is believed that the oil drag reduction mechanism differs from the water and air, mainly due to the viscosity effect as well as boundary layer condition. Experimental results indicate that drag reduction is possible with laminar flow, as shown with the microsized closed channel results presented earlier. This may be explained by the thin oil film concept, as illustrated in **Figure 22**. This model indicates that

during flow, oil becomes trapped and holds stationary between the Narrow riblets, and essentially lubricates the solid-liquid interface. The lubricating effect is believed to increase slip length (b), so therefore the flow velocity increases at the channel wall. A similar effect has been observed with the Pitcher plant (*Nepenthes genus*) peristome.[4,107] This was later demonstrated with the so-called biomimetic SLIPS[108] as well as rice leaf and butterfly wing effect surfaces.[24] Such an effect shows promise for drag reduction even with laminar flow.

5. Conclusions and Outlook

Sharks are able to move quickly through the water and remain fouling free due to microstructured riblets covering their skin. Such riblets efficiently reduce the skin friction drag by lifting and presumably pinning naturally occurring turbulent vortices. This minimizes the effects of transverse shear stress and momentum transfer present in turbulent flow. Lower drag translates to higher fluid flow velocity at the skin surface, so therefore microorganisms are unable to attach and the skin remains clean. This is further facilitated with the specially spaced riblets which do not allow larger microorganisms to colonize. Science's attempt to understand and mimic such unique shark skin structures has been the focus of many studies. Commericial applications for such low drag and antifouling surfaces are plentiful ranging from medical devices to marine vessels.
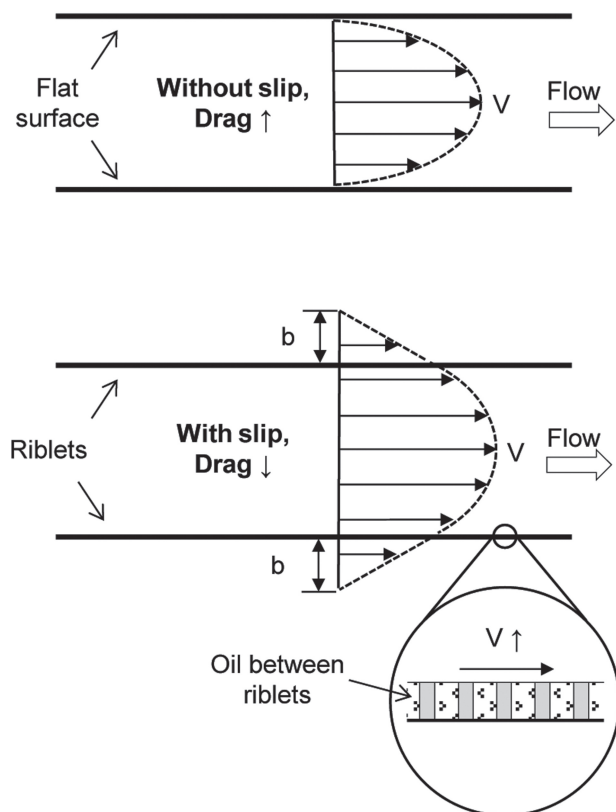
Riblet thin oil film model

Figure 22. Riblet thin oil film model. Appropriately sized riblets are believed to reduce drag by increasing the slip length *b* during laminar oil flow. Higher slip translates into lower drag and increased flow rate. Adapted with permission.[68] Copyright 2013, Royal Society of Chemistry.

Experiments attempting to unlock the secrets behind shark skin have included both open and closed channel flow, using a variety of blade, sawtooth, scalloped, and bullnose riblet geometries in continuous and segmented configurations. These have been studied with water, oil, and air in laminar through turbulent regimes. The majority of experimentation has been conducted with open channel flow. Such experiments measure drag with flat plates on force balances placed into water, oil, and air flows. Other experiments include airfoils in wind tunnels with drag measured by using wake traverses. More recently experiments have been conducted to measure drag via pressure drop reduction using riblet lined micro-sized closed channels. These experiments have provided greater insight to the role of neighboring wall effects and riblet drag reduction.

Riblets show an improved drag reduction in turbulent versus laminar flow, presumably due to the lifting and pinning of vortices. Results also indicate drag reduction improves in most cases with increasing Reynolds number (until expected plateauing). In open channel experiments, the maximum drag reduction up of 10% has been reported.[52] In closed channel experiments, maximum pressure drop reduction up to 34% has been reported.[67] Experiments using water, oil, and air also indicate that properly sized riblets combined with an appropriate

nanostructured coating further enhances drag reduction. Mechanisms include superhydrophobicity for water, improved smoothness for air, and superoleophilicity for oil flow.

Producing optimal and scalable drag reducing riblets for any fluid is believed to require the following design principles: low *h*, *t/s*, *t*, and *vw*; with $h/s = 0.5$, $s^+ \approx 15$, $H > 150$ wall units, blade geometry, and continuous configuration. In open and closed channel flow, riblets may be scaled up according to the fluid viscosity, where higher viscosity allows for larger riblets. Furthermore, microsized closed channel flow requires additional considerations, such as the vortices interaction between the neighboring walls. Such design principles are applicable for open and closed channel flow; thus providing new insight for various medical, marine, and industrial applications.

The outlook of riblet technology is promising for a variety of applications; however a few areas could be further explored to provide greater insight into riblet optimization. These include more research to fully understand the role of riblets with oil flow. The authors suspect that oleophobicity will enhance drag reduction, but this needs to be verified. Furthermore, additional computer analysis would be helpful to verify and possibly discover new optimal riblet geometries for a variety of fluids and flow conditions. Such analysis should include visualizing vortices interaction with riblets and one another. Finally, bioassay experiments would be useful to quantify the antifouling effects of low drag riblets.

Acknowledgements

[1] J. E. Gordon, *The new science of strong materials, or why you don't fall through the floor*, 2nd Ed., Pelican–Penguin, London, UK **1976**.

[2] *Design and Nature II Comparing Design in Nature with Science and Engineering* (Eds: M. W. Collins, C. A. Brebbia), WIT Press, Southampton, UK **2004**.

[3] *Learning from Nature How to Design New Implantable Biomaterials* (Eds: R. L. Reis, S. Weiner), Kluwer Academic Publishers, Norwell, MA **2004**.

[4] B. Bhushan, *Philos. Trans. R. Soc.* **2009**, *367*, 1445.

[5] B. Bhushan, *Biomimetics: Bioinspired Hierarchical-Structured Surfaces for Green Science and Technology*, Springer-Verlag, Heidelberg, Germany **2012**.

[6] *Bulletproof Feathers How Science Uses Nature's Secrets to Design Cutting Edge Technology*, (Ed: R. Allen), Ivy Press, London **2010**.

[7] *Bio-Inspired Innovation and National Security* (Eds: R. E. Armstrong, M. D. Drapeau, C. A. Loeb, J. J. Valdes), National Defense University Press, Washington, DC **2010**.

[8] Y. Bar-Cohen, *Biomimetics: Nature Based Innovation*, CRC Press, Boca Raton, FL **2011**.

[9] G. K. Batchelor, *An Introduction to Fluid Dynamics*, Cambridge University Press, Cambridge **1970**.

[10] R. D. Blevins, *Applied Fluid Dynamics Handbook*, Van Nostrand-Reinhold, New York **1984**.

[11] *Standard Handbook for Aeronautical and Astronautical Engineers* (Ed: M. Davies), McGraw-Hill, New York **2002**.

[12] F. White, *Viscous Fluid Flow*, 3rd ed., McGraw Hill, New York **2006**.

[13] R. W. Fox, A. T. McDonald, *Introduction to Fluid Mechanics*, 11th Ed. John Wiley & Sons, New York **2011**.

[14] *Industrial Biofouling Detection, Prevention and Control* (Eds: J. Walker, S. Surman, J. Jass), Wiley, New York **2000**.

[15] A. I. Railkin, *Marine Biofouling Colonization Processes and Defenses*, CRC Press, Boca Raton, FL **2004**.

[16] *Advances in Marine Antifouling Coatings and Technologies*, (Ed: C. Hellio, D. Yebra), CRC Press, Boca Raton, FL **2009**.

[17] F. J. Marentic, T. L. Morris, United States Patent no. 5, 133, 516, **1992**.

[18] J. L Kennedy, *Oil and gas pipeline fundamentals*, PennWell Books, Tulsa, OK **1993**.

[19] W. Brostow, *J. Indust. Eng. Chem.* **2008**, *14*, 408.

[20] B. Bhushan, Y. C. Jung, *Prog. Mater. Sci.* **2011**, *56*, 1.

[21] Z. Deyuan, L. Yuehao, C. Huawei, J. Xinggang, *Pipeline Gas J.* **2011**, March, 59.

[22] G. D. Bixler, B. Bhushan, *Philos. Trans. R. Soc. A* **2012**, *370*, 2381.

[23] B. Bhushan, Y. C. Jung, K. Koch, *Philos. Trans. R. Soc. A* **2009**, *367*, 1631.

[24] G. D. Bixler, B. Bhushan, *Soft Matter* **2012**, *8*, 11271.

[25] E. D. Burger, W. R. Munk, H. A. Wahl, *J. Pet. Technol.* **1982**, *34*, 377.

[26] R. Martínez-Palou, M. Mosqueira, B. Zapata-Rendón, E. Mar-Juárez, C. Bernal-Huicochea, J. Clavel-López, J. Aburto, *J. Pet. Sci. Eng.* **2011**, *75*, 274.

[27] *Nanotechnology in Biology and Medicine* (Ed: T. Vo-Dinh) CRC Press, Boca Raton, FL **2007**.

[28] *Nanomedicine Design of Particles, Sensors, Motors, Implants, Robots, and Devices* (Eds: M. J. Schulz, V. N. Shanov, Y. Yun), Artech House, Boston, MA **2009**.

[29] *The Role of Biofilms in Device-Related Infections* (Eds: M. Shirtliff, J. G. Leid), Springer-Verlag, Berlin **2009**.

[30] *Biofouling Types, Impact and Anti-Fouling* (Eds: J. Chan, S. Wong), Nova Science Publishers, New York **2010**.

[31] M. Copisarow, *Science* **1954**, *101*, 406.

[32] Anon, Marine Fouling and its Prevention, Woods Hole Oceanographic Institute, US Naval Institute, Annapolis, USA **1952**.

[33] *Marine Boring and Fouling Organisms*, (Ed: D. L. Ray), University of Washington Press, Seattle **1959**.

[34] *Fouling Science and Technology*, (Ed: L. F. Melo, T. R. Bott, C. A. Bernardo), Kluwer Academic Publishers, Dordrecht, The Netherlands **1988**.

[35] *Fouling of Heat Transfer Equipment*, (Ed: E. F. C. Somerscales, J. G. Knudsen), Hemisphere Publishing Corporation, Washington, DC **1981**.

[36] W. Barthlott, C. Neinhuis, *Planta* **1997**, *202*, 1.

[37] A. Kesel, R. Liedert, *Comp. Biochem. Physiol. A* **2007**, *146*, S130.

[38] E. Ralston, G. Swain, *Bioinspiration Biomimetics* **2009**, *4*, 1.

[39] D. W. Bechert, G. Hoppe, W. E. Reif, Paper # AIAA-85-0546, presented at *AIAA Shear Flow Control Conference*, Boulder, CO, AIAA, New York **1985**.

[40] D. W. Bechert, M. Bruse, W. Hage, R. Meyer, Paper # AIAA-1997-1960, presented at *AIAA 28th Fluid Dynamics Conference*, Snowmass Village, CO, AIAA, New York **1997**.

[41] D. W. Bechert, M. Bruse, W. Hage, R. Meyer, *Naturwissenschaften* **2000**, *87*, 157.

[42] B. Dean, B. Bhushan, *Philos. Trans. R. Soc.* **2010**, *368*, 4775.

[43] W. Reif, *Courier Forschungsinstitut Senckenberg*, Frankfurt, Germany, **1985**, *78*, 1.

[44] J. F. Schumacher, N. Aldred, M. E. Callow, J. A. Finlay, J. A. Callow, A. S. Clare, A. B. Brennan, *Biofouling* **2007**, *23*, 307.

[45] A. J. Scardino, in *Advances in Marine Antifouling Coatings and Technologies* (Eds: C. Hellio, D. Yebra), CRC Press, Boca Raton, FL **2009**.

[46] A. B. Brennan, R. H. Baney, M. I. Carman, T. G. Estes, A. W. Feinberg, L. H. Wilson, J. F. Schumacher, United States Patent no. 7, 650, 848, **2010**.

[47] L. W. Reidy, G. W. Anderson, Paper # AIAA-1988-0138, presented at *26th AIAA Aerospace Sciences Meeting*, Reno, NV, AIAA, New York **1988**.

[48] M. C. Gillcrist, L. W. Reidy, in *Drag Reduction in Fluid Flows* (Eds: R. H. J. Sellin, R. T. Moses), Elis Horwood Publishers, Chichester, UK **1989**.

[49] M. J. Walsh, *Aircraft* **1990**, *27*, 572.

[50] D. Neumann, A. Dinkelacker, *Appl. Sci. Res.* **1991**, *48*, 105.

[51] J. J. Rohr, G. W. Andersen, L. W. Reidy, E. W. Hendricks, *Exp. Fluids* **1992**, *13*, 361.

[52] D. W. Bechert, M. Bruse, W. Hage, J. G. T. van der Hoeven, G. Hoppe, *J. Fluid Mech.* **1997**, *338*, 59.

[53] D. W. Bechert, M. Bruse, W. Hage, *Exp. Fluids* **2000**, *28*, 403.

[54] C. C. Buttner, U. Schulz, *Smart Mater. Struct.* **2011**, *20*, 1.

[55] R. Gurneberger, W. Hage, *Exp. Fluids* **2011**, *50*, 363.

[56] M. J. Walsh, Paper # AIAA-1982-0169, presented at *AIAA 20th Aerospace Sciences Meeting*, Orlando FL, AIAA, New York **1982**.

[57] M. J. Walsh, A. M. Lindemann, Paper # AIAA-1984-0347, presented at *AIAA 22nd Aerospace Sciences Meeting*, Reno, NV, AIAA, New York **1984**.

[58] S. P. Wilkinson, B. S. Lazos, in *Turbulence Management and Relaminarisation* (Eds: H. W. Liepman, R. Narasimha), Springer-Verlag, Berlin **1988**.

[59] E. Coustols, Paper # AIAA-89-0963, presented at *AIAA Shear Flow Conference*, Tempe, AZ, AIAA, New York **1989**.

[60] N. Subaschandar, R. Kumar, S. Sundaram *J. Aircraft* **1999**, *36*, 890.

[61] P. R. Viswanath, Paper # AIAA-99-3402, presented at the *AIAA 30th Fluid Dynamics Conference*, Norfolk, VA, AIAA, New York **1999**.

[62] P. R. Viswanath, *Prog. Aerospace Sci.* **2002**, *38*, 571.

[63] M. Han, H. C. Lim, Y.-G. Jang, S. L. Seung, S.-J. Lee, Paper # 0-7803-7731-1, presented at *12th International Conference on Solid State Sensors*, Actuators and Microsystems, Boston, MA **2003**.

[64] A. Sareen, R. W. Deters, S. P. Henry, M. S. Selig, Paper # AIAA-2011-558, presented at *49th AIAA Aerospace Sciences Meeting*, Orlando, FL, AIAA, New York **2011**.

[65] K. N. Liu, C. Christodoulou, O. Riccius, D. D. Joesph, *Am. Inst. Aeronaut. Astronaut. J.* **1990**, *28*, 1697.

[66] Y. C. Jung, B. Bhushan, *J. Phys.: Condens. Matter* **2010**, *22*, 1.

[67] G. D. Bixler, B. Bhushan, *J. Colloid Interface Sci.* **2013**, *393*, 384.

[68] G. D. Bixler, B. Bhushan, *Soft Matter* **2013**, *9*, 1620.

[69] P. Nitschke, *Max-Planck Institute for Stromungsforschung*, Gottingen, West Germany, **1983**.

[70] G. V. Enyutin, Y. A. Lashkov, N. V. Samoilova, *Fluid Dyn.* **1995**, *30*, 45.

[71] K. Krieger, *Science* **2004**, *305*, 636.

[72] R. J. Kline, W. C. Reynolds, F. A. Schraub, P. W. Runstadler, *J. Fluid Mech.* **1967**, *30*, 741.

[73] B. Munson, D. Young, T. Okiishi, *Fundamentals of Fluid Mechanics*, 5th Ed., Wiley, New York **2005**.

[74] P. Lowrey, J. Harasha, *Energy* **1991**, *16*, 631.

[75] P. Luchini, F. Manzo, A. Pozzi, *J. Fluid Mech.* **1991**, *228*, 87.

[76] S. J. Lee, S. H. Lee, *Exp. Fluids* **2001**, *30*, 153.

[77] J. Oeffner, G. V. Lauder, *J. Exp. Biol.* **2012**, *215*, 785.

[78] S. P. Wilkinson, Paper #AIAA-1983-0294, presented at the *21st Aerospace Sciences Meeting of the American Institute of Aeronautics and Astronautics*, Reno, NV, AIAA, New York **1983**.

[79] D. W. Bechert, G. Hoppe, J. G. T. van der Hoeven, R. Makris, *Exp. Fluids* **1992**, *12*, 251.

[80] M. J. Walsh, *Prog. Astronaut. Aeronaut.* **1990**, *123*, 203.

[81] P. S. Jang, D. J. Benney, R. L. Gran, *J. Fluid Mech.* **1986**, *169*, 109.

[82] J. M. Caram, A. Ahmed, *Am. Inst. Aeronaut. Astronaut. J.* **1991**, *29*, 1769.

[83] S. Sundaram, P. R. Viswanath, N. Subaschandar, *Am. Inst. Aeronaut. Astronaut. J.* **1999**, *37*, 851.

[84] S. Sundaram, P. R. Viswanath, S. Rudrakumar, *Am. Inst. Aeronaut. Astronaut. J.* **1996**, *34*, 676.

[85] K. K. Wetzel, S. Farokhi, Paper # AIAA-1996-2428-CP, presented at the *AIAA 14th Applied Aero-dynamics Conference*, New Orleans, LA, AIAA, New York **1996**.

[86] P. R. Viswanath, R. Mukund, *Am. Inst. Aeronaut. Astronaut. J.* **1995**, *33*, 945.

[87] E. Coustols, V. Schmitt, in *Turbulence Control by Passive Means* (Ed: E. Coustols), Kluwer, Dordrecht, The Netherlands **1990**.

[88] E. Coustols, J. Cousteix, *Am. Inst. Aeronaut. Astronaut. J.* **1994**, *32*, 431.

[89] B. Dean, B. Bhushan, *Appl. Surf. Sci.* **2012**, *258*, 3936.

[90] B. Denkena, J. Kohler, B. Wang, *CIRP J. Manuf. Sci. Tech.* **2010**, *3*, 14.

[91] G. Hirt, M. Thome, *Prod. Eng. Res. Devel.* **2007**, *1*, 351.

[92] P. H. Dickinson, G. M. Proudley, United States Patent no. 4, 994, 639, **1991**.

[93] J. Ou, B. Perot, J. P. Rothstein, *Phys. Fluids* **2004**, *16*, 4635.

[94] R. J. Daniello, N. E. Waterhouse, J. P. Rothstein, *Phys. Fluids* **2009**, *21*, 085103.

[95] M. B. Martell, J. B. Perot, J. P. Rothstein, *J. Fluid Mech.* **2009**, *620*, 31.

[96] M. B. Martell, J. P. Rothstein, J. B. Perot, *Phys. Fluids* **2010**, *22*, 065102.

[97] J. Genzer, K. Efimenko, *Biofouling* **2006**, *22*, 339.

[98] D. Ebert, B. Bhushan, *J. Colloid Interface Sci.* **2012**, *384*, 182.

[99] D. Ebert, B. Bhushan, *Langmuir* **2012**, *28*, 11391.

[100] J. M. Caram, A. Ahmed, *Am. Inst. Aeronaut. Astronaut. J.* **1992**, *30*, 2817.

[101] J. D. Lee, G. M. Gregorek, K. D. Korkan, Paper # AIAA-1978-1118, presented at 11th *Fluid and Plasma Dynamics Conference*, Seattle, WA, AIAA, New York **1978**.

[102] J. B. Barlow, W. H. Rae, A. Pope, *Low-Speed Wind Tunnel Testing*, 3rd Ed., Wiley-Interscience, New York **1999**.

[103] J. D. Anderson, *Fundamentals of Aerodynamics*, 5th Ed., McGraw Hill, New York **2010**.

[104] Wing Design, www.allstar.fiu.edu, (December, 2012).

[105] *Pilot's Encyclopedia of Aeronautical Knowledge, United States Federal Aviation Administration*, Skyhorse, New York **2007**.

[106] K. Gompertz, J. P. Bons, J. W. Gregory, Paper # AIAA-2012-0678, presented at 50th *AIAA Aerospace Sciences Meeting*, Nashville, TN, AIAA, New York **2012**.

[107] K. Koch, W. Barthlott, *Philos. Trans. R. Soc.* **2009**, *367*, 1487.

[108] T.-S. Wong, S. H. Kang, S. K. Y. Tang, E. J. Smythe, B. D. Hatton, A. Grinthal, J. Aizenberg, *Nature* **2011**, *477*, 443.